Data-driven analysis of COVID-19 reveals specific severity patterns distinct from the temporal immune response

Jackwee Lim[1,15], Kia Joo Puan[1,15], Liang Wei Wang[1,15], Karen Wei Weng Teng[1], Chiew Yee Loh[1], Kim Peng Tan[1], Guillaume Carissimo[1,2], Yi-Hao Chan[1,2], Chek Meng Poh[1,2], Cheryl Yi-Pin Lee[1,2], Siew-Wai Fong[1,2,7], Nicholas Kim-Wah Yeo[1,2], Rhonda Sin-Ling Chee[1,2], Siti Naqiah Amrun[1,2], Zi Wei Chang[1,2], Matthew Zirui Tay[1,2], Anthony Torres-Ruesta[1,2,9], Norman Leo Fernandez[1], Wilson How[1], Anand K. Andiappan[1], Wendy Lee[1], Kaibo Duan[1], Seow-Yen Tan[10], Gabriel Yan[11], Shirin Kalimuddin[12,13], David Chien Lye[3,4,5,6], Yee-Sin Leo[3,4,5,6,8], Sean W. X. Ong[3,4], Barnaby E. Young[3,4,5], Laurent Renia[1,2,16], Lisa F.P. Ng[1,2,9,14,16,*], Bernett Lee[1,16], Olaf Rötzschke[1,16,17,*]

[1]Singapore Immunology Network, Agency for Science, Technology and Research, 8A Biomedical Grove, Immunos, Singapore 138648

[2]A*STAR Infectious Disease Labs, Agency for Science, Technology and Research, 8A Biomedical Grove, Immunos, Singapore 138648

[3]National Centre for Infectious Diseases, 16 Jalan Tan Tock Seng, Singapore 308442, Singapore

[4]Department of Infectious Diseases, Tan Tock Seng Hospital, 11 Jalan Tan Tock Seng, Singapore 308433, Singapore

[5]Lee Kong Chian School of Medicine, Nanyang Technological University, 11 Mandalay Road, Singapore 308232, Singapore

[6]Yong Loo Lin School of Medicine, National University of Singapore and National University Health System, 10 Medical Drive, Singapore 117597, Singapore

[7]Department of Biological Sciences, National University of Singapore

[8]Saw Swee Hock School of Public Health, National University of Singapore and National University Health System, 12 Science Drive 2, #10-01, Singapore 117549, Singapore

[9]Department of Biochemistry, Yong Loo Lin School of Medicine, National University of Singapore, 8 Medical Drive, Singapore 117596, Singapore

[10]Department of Infectious Diseases, Changi General Hospital, 2 Simei Street 3, Singapore 529889, Singapore

[11]Department of Medicine, National University Hospital, 5 Lower Kent Ridge Road, Singapore 119074, Singapore

[12]Department of Infectious Diseases, Singapore General Hospital, Academia Level 3, 20 College Road, Singapore 169856, Singapore

[13]Emerging Infectious Diseases Program, Duke-NUS Medical School, 8 College Road, Singapore 169857, Singapore

[14]Institute of Infection, Veterinary and Ecological Sciences, University of Liverpool, Liverpool, 8 West Derby Street, Liverpool, L7 3EA, United Kingdom

[15]First authors

[16]Senior authors

[17]Lead Contact

*Correspondence: olaf_rotzschke@immunol.a-star.edu.sg (O.R.); lisa_ng@immunol.a-star.edu.sg

Keywords:

SARS-CoV-2, COVID-19, mass cytometry, CyTOF, Quanterix, Luminex, inflammation

Abstract

Key immune signatures of SARS-CoV-2 infection may associate with either adverse immune reactions (severity) or simply an ongoing anti-viral response (temporality); how immune signatures contribute to severe manifestations and/or temporal progression of disease and whether longer disease duration correlates with severity remain unknown. Patient blood was comprehensively immunophenotyped via mass cytometry and multiplex cytokine arrays, leading to the identification of 327 basic subsets that were further stratified into more than 5000 immunotypes and correlated with 28 plasma cytokines. Low-density neutrophil abundance was closely correlated with hepatocyte growth factor levels, which in turn correlated with disease severity. Deep analysis also revealed additional players, namely conventional type 2 dendritic cells, natural killer T cells, plasmablasts and $CD16^{+}$ monocytes, that can influence COVID-19 severity independent of temporal progression. Herein, we provide interactive network analysis and data visualization tools to facilitate data mining and hypothesis generation for elucidating COVID-19 pathogenesis.

Introduction

The pandemic coronavirus disease 2019 (COVID-19) is caused by the severe acute respiratory syndrome coronavirus 2 (SARS-CoV-2). As of 25th January 2021, there are 100 million cases with more than 2 million deaths worldwide (Dong et al., 2020). While the immunogenic responses in COVID-19 vaccinated individuals remain largely unknown, the majority of the COVID-19 patients are asymptomatic or have mild flu-like symptoms, some develop severe diseases, which may lead to death from respiratory failure or even multi-organ failure from a hyperactivated immune system (Manson et al., 2020). The immunopathology in severe COVID-19 is characterized by lymphopenia, a sustained loss of $CD4^+$ and $CD8^+$ T cells, a dramatic increase in the number of immature neutrophils as well as an altered myeloid cell compartment in severe COVID-19 cases (Carissimo et al., 2020; Jouan et al., 2020; Kuri-Cervantes et al., 2020; Silvin et al., 2020). Another hallmark of severe COVID-19 is the cytokine storm associated with elevated levels of cytokines (IL1β, IL1Rα, IL2, IL7, IL10, G-CSF, TNFα), chemokines (IP10, MCP1, MIP1α) and endogenous neutrophil calprotectin (Ragab et al., 2020; Silvin et al., 2020; Barnaby E. Young et al., 2020).

Although many studies have independently identified different immunotypes and cytokines associated with SARS-CoV-2 infection and severe COVID-19, their interplay is still largely unknown for distinguishing active infection, severity and post-infection aberrations. In this work, we analyzed the blood samples of 77 hospitalized patients and 10 healthy controls. Also, to obtain a more full-bodied approach, we have compiled the data and provided a comprehensive COVID-19 resource, which integrates high dimensional mass cytometry and bead-based cytokine/chemokine arrays. Network analyses between the key immune subsets and the associated cytokine levels in the plasma were used to correlate clinical states and disease trajectory of COVID-19. One of the key findings is the identification of a link between hepatocyte growth factor (HGF) and low-density neutrophils (LD Neu). While both factors are closely associated with disease severity, it represents only the tip of the iceberg; the network of underlying pathways is complex and involves many players. By sharing these data

97 together with easy-to-use visualization tools, we provide a rich resource to study the
98 manifestation of COVID-19 as well as the particulars of the SARS-CoV-2 induced immune
99 response.

Results

Study design and clinical characteristics of the cohort

To determine the changes induced by SARS-CoV-2 infection in peripheral blood mononuclear cell (PBMC) subsets, we assembled a comprehensive mass cytometry panel of 40 antibodies against lineage-specific markers, adhesion molecules and other surface molecules indicative of the functional state of the cells (Figure 1A). This panel divided the entire PBMC population into 327 partly overlapping subsets, which consisted of both extensively described immune cell populations such as T cells, B cells, dendritic cells, monocytes, natural killer (NK) cells, basophils, mucosal-associated invariant T (MAIT) cells, innate lymphoid cells (ILCs) and LD Neu, as well as lesser-known immune cell populations such as $CD56^{+}$ monocytes, $CD56^{+/-}$ MAIT and the PD-$L1^{+}$ LD Neu subsets (Villani et al., 2017). Cytokine bead arrays based on Luminex™ and ultra-sensitive Quanterix™ technologies were used to quantify the changes of twenty-eight cytokines in patient plasma (Figure 1A). The interconnected databases generated by these approaches were then subjected to network analysis to determine immune signatures of the anti-SARS-CoV-2 response as well as the cellular and molecular drivers of severe COVID-19.

In order to establish a timeline on the SARS-CoV-2 specific immune response, 87 blood samples were collected from 77 hospitalized COVID-19 patients at varying time points (Figure 1B). The state of infection was determined by SARS-CoV-2 real-time reverse transcriptase polymerase chain reaction (PCR) as previously described (Corman et al., 2020; Barnaby E Young et al., 2020). PCR positive samples were grouped into early active (median days post illness onset (PIO): 9) and late active (median days PIO: 20). PCR negative samples were grouped into early convalescence (median days PIO: 25) and late convalescence (median days PIO: 39) (Figure 1B). As a proxy for disease severity, the samples were stratified based on treatment regime into three severity groups, namely mild (symptomatic; n = 32), moderate (symptomatic with supplemental oxygen (suppl. O_2); n = 24) and severe (suppl. O_2 and need for intensive care unit (ICU); n = 31). With the exception of

age and gender, most demographic variables did not differ significantly between COVID-19 patients and healthy donors, as well as between severity groups (Table S1). Severity was associated with advanced age ($p < 0.0001$).

Temporal variations in PBMC subsets during active and convalescent COVID-19

Mass cytometry analysis allowed gating of total PBMCs into 38 non-overlapping basic subsets from both the adaptive and innate arms of the immune system (Figure 2A and Table S2). Uniform Manifold Approximation and Projection (UMAP) analysis segregated these cells into distinct clusters of T cells, B cells, NK cells, monocytes and other antigen presenting cells (Figure 2A, left). Surprisingly, large numbers of LD Neu were detected (Figure 2A, right). Neutrophils are typically not present in the PBMC fraction of healthy donors but found in abundance in COVID-19 samples. Subsequent analysis with a targeted mass cytometry panel confirmed that these cells are indeed LD Neu by revealing an immunophenotype that is consistent with neutrophils ($CD66b^{+}CD15^{+}CD16^{high}CD10^{+}CD24^{+}$) (Table S2).

Generalized lymphopenia was observed in the active phase relative to convalescent COVID-19 (Figure 2A, right), particularly in various $CD4^{+}$ and $CD8^{+}$ T cell, most B cell, NKT and MAIT cell subsets. A significant reduction was also observed for non-classical monocytes (NC. Mono), while increased frequencies were detected for plasmablasts, classical monocytes (C. Mono) and LD Neu. Closer inspection of the temporal profiles for various subsets revealed a number of interesting trends (Figure 2B). For LD Neu, the increase was largely restricted to the late active phase, while the plasmablast frequency increased during the early active phase. The frequency of C. and intermediate (Int.) monocytes rose throughout active infection before declining in the convalescent phase. In contrast, the frequency of NC. Mono in the blood dropped sharply during the early active phase but increased gradually until late convalescence (Figure 2B).

The timeline of events is particularly evident in a heatmap display (Figure 3A, left). Based on the increase in subset frequencies, the earliest responders were NK cells followed

by plasmablasts, C./Int. Mono and LD Neu. Further, there was also a sharp decrease in numbers, which may indicate the mobilization of subsets such as NC. Mono, T regulatory (Treg), T follicular helper (T_{FH}) and $CD4^+$ T cells to the lung mucosa as front-line responses. Their frequencies increased later during convalescence (Figures 2B and 3A). We also observed a loss in blood MAIT cell frequency during active infection that was restored to healthy levels during convalescence (Figure 3A), which is in line with a previous study suggesting active recruitment of MAIT to the lung mucosa (Parrot et al., 2020). Also the robust increase in the frequency of circulating plasmablasts during the active phase is consistent with previous single-cell analysis of patients with severe COVID-19 (Wilk et al., 2020). In contrast, non-class-switched memory (NSM), class-switched memory (CSM) and IgM^+ memory B cells showed decreased frequencies, which increased during convalescence but did not recover to healthy levels.

Activation and differentiation of immune cells during the course of the SARS-CoV-2 infection were indicated by changes in the expression levels of surface markers (Figure 3A, right). The profiles of more than 5000 immunotypes derived from the 38 basic immune subsets can be assessed by an interactive online viewer (see Materials and Methods: Data and Code Availability and Table S2). Although expression of functional markers was highly heterogeneous across immune subsets and disease phases, we observed some notable trends. CD38 was upregulated across diverse immune subsets during active infection, indicative of widespread cell activation in response to viral infection. CD169, an adhesin that binds sialic acid, was also selectively upregulated in all monocyte subsets during the early but not late active phase. Many T and B cell subsets – Treg TEM, NSM and CSM cells – downregulated the lymph node homing molecule CCR6 over the course of disease, primarily during active infection, which may impede homing to inflamed tissues and development of germinal center responses (Figure S1). A range of cell subsets exhibited elevated levels of CD57 from early active infection to early convalescence, indicative of immune senescence

(Figure 3A). Finally, CD16 (FcγRIII) was upregulated on MAIT cells in late active infection and on LD Neu, all monocyte subsets and $CD16^+$ NK cells during convalescence (Figure 3A).

Based on the observed phenotype variations, we defined and curated 327 partly overlapping immunotypes and compared the frequencies of these subsets in each phase of COVID-19 (Figure 3B and Table S3). High levels of $CD169^+$ C. Mono were observed exclusively during early active infection. The same also applied for $CD38^{high}$ plasmacytoid dendritic cell (pDC) subsets and IgA^+ plasmablasts, followed by IgA^- plasmablasts. Notably, four subsets of monocytes, namely $CD141^+HLADR^-$ C. Mono, $CD56^+$ C. Mono, $CD45RA^-$ Int. Mono and $CD56^+$ Int. Mono peaked during late active SARS-CoV-2 infection and may portend recovery (Figure 3B). The increase in the LD Neu population from early to late active infection is reflected in both its $PD\text{-}L1^+$ and $CD5^+$ subsets. The active-phase lymphopenia affected virtually all $CD8^+$ central (CD8 TCM) and effector memory T subsets (CD8 TEM) (Figure 3B). Significant losses of $CD56^+CD8^+$ MAIT, $CCR6^+$ CSM, $HLA\text{-}DR^+CD38^-$ $CD4^+$ T, $CD57^-CD8^+$ and NKT subsets were also observed during active infection (Figure 3B). Next, in convalescence, a frequency increase persisting into late phase was observed for T cells (such as $CD57^+CD4^+$ T, $HLA\text{-}DR^+CD38^+$ $CD8^+$ T, $CD38^+/ICOS^+$ T_{FH} defined as circulatory $CXCR5^+$, Treg TCM/TEM), NC. Mono (IgA^+, $CD45RO^-$ and $CD16^+CD169^+$) and $CCR6^-$ CSM above healthy levels. Also in this phase, the loss of $CD5^-$ conventional type 2 DC (cDC2), Vδ2 TCM, Vδ2 TEM, B cells memory $CXCR5^+$, $CCR6^+$ CSM and $CD5^-$ transitional B cells persisted into late convalescence below healthy levels (Figure 3B). These late-convalescent immunotypes, which do not recover to healthy levels, may represent post-infection aberrations.

Alterations of immunotypes associated with disease severity

Depending on the treatment given, active and convalescent patients were stratified into 'mild' (symptomatic), 'moderate' (symptomatic with suppl. O_2) and 'severe' (suppl. O_2 and ICU admission). Thus we obtained groups I, II and III denoting active mild, active moderate, and active severe, respectively and groups IV (severe), V (moderate), and VI (mild) for patients

in the convalescent phase (Figure 1A). The global changes in the cell subset composition are particularly evident in UMAP plots colored according to the fold change in reference to healthy controls (Figure 3A). The most striking association was observed for LD Neu. While a minor increase was observed in group I (active, mild), the numbers increased dramatically in group II (active, moderate) and peaked in group III (active, severe). The numbers persisted in group IV (conv., severe) and gradually declined from group V (conv., moderate) to group VI (conv., mild) (Figures 4A, 4B and S2A). This was also reflected in the increased LD Neu-to-lymphocyte ratios compared with group VI mild convalescent and healthy (Figure S3A). The expansion of LD Neu was due to $CD16^{+}$ neutrophils and $CD16^{high}$ neutrophils. $CD16^{high}$ neutrophils (Figures S3B and S3C) described herein resemble pseudo-Pelger-Huet cells, which were previously reported in other severe viral infections (Morrissey et al., 2020).

Two other immune cell subsets, which closely associated with severe COVID-19 are Vδ2 T and NKT cells (Figures 4B and S2A). Their frequencies sharply declined in group II/III/IV patients. Further analysis revealed that the loss of Vδ2 T is likely due to Vδ2 TCM and Vδ2 TEM, which remained significantly reduced in frequency in groups IV/V compared with healthy (Figures 4B, 5A and S4A). Similarly for NKT sub-populations, the $CD57^{-}$ NKT cell but not $CD57^{+}$ NKT cell subset was reduced in frequency in groups II/III/IV (Figure S4D). The loss of the $CD57^{-}$ NKT cells included the $CD4^{+}$, $CD8^{+}$ and the double-negative (DN) NKT sub-populations. Although reduced numbers were also detected for dendritic cell subsets, the frequencies of pDC and cDC2 were only marginally suppressed across groups II/III/IV/V (Figures 4B, S4B and S4C). For plasmablasts, a subtle increase in frequency was observed in the active phase groups I to III but waned during convalescence (Figures 4A, 4B, S5A, and S5B). Notably, IgA^{-} plasmablasts showed a higher increase compared with its IgA^{+} counterpart (6.53-fold vs 2.89-fold compared with HD) in group III (Figures 4B and S5B).

Among the T cells, the strongest association with severity was observed for $HLADR^{+}CD38^{+}$ $CD8^{+}$ T cells. Unlike the frequencies of MAIT and NK cell subsets across groups I/II/III and groups IV/V/VI, which were largely invariant across groups and thus did not

associate with severity (Figures S6A and S6B). The numbers of hyperactivated HLADR^{+}CD38^{+} CD8^{+} T cells peaked in severity groups III/IV, whereby the highest frequency was detected in group IV during convalescence (Figures 4B and S7A). Also, a number of emerging studies suggested a role of inflammatory monocytes in the pathogenesis of COVID-19. In line with these results, although our data also showed elevated numbers of C. Mono and Int. Mono during the active phase, the increase with regard to severity was only marginal. The reverse trend was evident for NC. Mono, which declined in the active groups I/II/III but increased during convalescence (Figures 4B, 5A, S2A and S3D).

The association of the frequencies of the 38 basic immune subsets with the six severity groups as well as the associated surface marker expression is summarized in Figure S2. Their phenotypes can be assessed by using the online viewer (see Materials and Methods: Data and Code Availability). Figure 5A shows the subsets out of the 327 common immunotypes, which exhibited the most significant frequency changes with regard to the six severity groups. Based on the frequency distribution, they were divided into five different clusters (Figure 5A, left). Immune subsets in the first cluster positively associated with mild infection such as CD161^{+} NKT and CD5^{+} cDC2, which only increased in group I and may thus play a potential protective role (Figure 5A). The second cluster is positively associated with active SARS-CoV-2 infection across mild to severe groups I/II/II. Besides the plasmablasts, CD169^{+}/CD38^{+} C. Mono and CD86^{+}/CD45RA^{-}/CD38^{+} Int. Mono but not total monocytes remained elevated in groups II/III. Also, like CD169^{+} C. Mono, both CD38^{high}CD45RA^{+} pDC and HLA-DR^{+}CD56^{DIM} NK peaked in group I and remained high in groups II/III above healthy levels. Notably, HLA-DR^{Low}CD141^{+} C. Mono, which has been reported to be over-represented in ICU patients did not show a pronounced association with the most severe group III but was rather increased throughout the active phase (Silvin et al., 2020). This suggests that the aforementioned subset is unlikely to be a marker for severity. The third cluster is positively associated with severe COVID-19. In this cluster, CXCR5^{+} B cells memory subset was only increased in more severe groups II/III but various LD Neu

subsets were elevated in both severity groups III and IV (Figures 5A and 5B). PD-L1^{+} LD Neu are most abundant in groups II/III while CD5^{+} LD Neu peaked in group IV. Within group IV, hyperactivated HLA-DR^{+}CD38^{+} CD8^{+} T cell subset was also elevated (Figures 5A and,5B). The fourth cluster consisted of mixed frequency distribution during convalescence. Various NC. Mono subsets (CD38^{+}/CD123^{+}/CD86^{+}/CD45RO^{-}/IgA^{+}) and Treg TEM and T_{FH} subsets were increased in frequencies across groups IV/V/VI above healthy levels (Figures 5A and S3G). On the other hand, immune subsets of MAIT, CSM and NSM of more severe COVID-19 patients often did not recover to healthy levels. Finally, the fifth cluster defined as "severe inverse" included subsets exhibiting the greatest loss in frequency in patients with most severe but not mild COVID-19. These were mostly cDC2, CD45RA^{+} pDC, CD57^{-} NKT and Vδ2 memory T cells, which may indicate direct involvement in COVID-19 related pathology (Figures 5A and S4).

The shifts in surface marker co-expression for some of the key populations are also shown in Figure 5B. For LD Neu, besides the IgA^{+} marker, the PD-L1 co-expression was particularly pronounced across the active and convalescent groups II to V. Additionally, CD16^{high} LD Neu was more abundantly expressed during convalescence, which was not seen in healthy donors (Figures 5B and S3C). Similarly for NC. Mono, besides IgA^{+} and CD86^{+} markers, CD16 co-expression was strongly increased in convalescent phase groups IV and V (Figures 5B, S3E and S3G). And for hyperactivated HLA-DR^{+}CD38^{+} CD8^{+} T cells, the co-expression of CD45RO marker was highly elevated in groups III and IV. Similarly, a concomitant increase in the co-expression of CD11b^{+} and CD24^{+} markers by CD56^{dim}NK was particular evident in groups III and IV (Figures 5B and S2B). Notably, this specific immunotype has been reported to transdifferentiate into myeloid cells e.g. neutrophils (Song et al., 2020).

Dynamics of plasma cytokine levels in COVID-19 patients

In order to correlate the shifts in frequency and phenotype with the cytokine/chemokine environment, we have screened the corresponding COVID-19 plasma samples for 28

analytes using either Luminex or high-sensitivity Quanterix bead arrays. Of these, thirteen cytokines showed statistically significant associations with the six severity groups (adjusted $p < 0.05$) (Figure 6A). A comparison between the association with severity and the timing of the immune response revealed that IFNα, while abundantly found in the early active phase, had very little prognostic value with regard to severity (Figure 6B). While the levels of IL6 seem to better match disease severity, this applied only for the active phase. Also, IL6 was mostly detected during the early active phase. The association with severity however substantially improved for IP10, TNFα, HGF and VEGF-A. Especially the latter two were detected in similar extent during both the active and convalescent phases.

To further identify the cytokine/immune cell associations during SARS-CoV-2 infection, we first correlated the cytokine levels with the frequencies of the 327 immunotypes. The various plots for these correlations can be assessed in an interactive online viewer (see Materials and Methods: Data and Code Availability). As the immune responses in different phases of infection are vastly different, we carried out separate correlations for the active and convalescent phases (Figure 6C, top). During active infection, IFNα, IP10, IL6 and HGF showed a pleiotropic effect on a variety of immune cells. IFNα had a negative correlation with various monocyte subsets such as NC. Mono but positively associated with ILC2, $CD38^+$ Vδ2 TCM, IgM^+CD38^{high} B cells, $CD5^-$ transitional B cells, $CCR6^-$ transitional B cells and $CD25^+$ ILCs. IL6 was positively associated with B cells and various plasmablast subsets, and HGF was positively associated with LD Neu but negatively with NKT.

During convalescence, a greater number of cytokines was associated with various immunotypes, albeit the association was typically weaker as compared to the active phase (Figure 6C, bottom). VEGF-A was strongly associated with $HLA\text{-}DR^+CD38^+$ $CD8^+$ T cells but negatively with $CD8^+CD56^-$ MAIT cells. Interestingly, IgA^+, $CD5^+$ and $PD\text{-}L1^+$ LD Neu positively associated with TNFα, which is known to promote neutrophil degranulation (Cross et al., 2008; Salamone et al., 2001). Additionally, PIGF1 and IL17A positively associated with $CD38^+$ NKT and $CXCR5^-$ B cells, respectively, while negative associations of both

proinflammatory TNFα and HGF with Vδ2 T cells were observed, as well as negative associations of both IL6 and HGF with $CD8^{+}CD56^{-}$MAIT.

As cytokines can also directly influence the surface expression of biomarkers, we carried out a similar correlation for the surface molecules detected during the active phase on the 327 immunotypes (Figure 6D). While there were fewer cytokines found significant, they often correlated with the same surface marker on a number of different cell subsets. IFNα was positively associated with upregulated $CD169^{+}$ on both C. and Int. Mono. The same cytokine also triggered the upregulation of CD38 on various NC. Mono as well as $CD141^{-}CD11b^{-}$ C. Mono and various B cell subsets. IFNα was also found negatively associated with CD86 on B cells, while IL6 was negatively associated with CD4 on various C. Mono populations. HGF was strongly associated only with the transdifferentiating $CD11b^{+}CD56^{dim}$ NK cells, which expressed CD24 (Song et al., 2020). Also, these data can be visualized using the online viewer (see Materials and Methods: Data and Code Availability).

Integrated network analysis of immune subsets and plasma cytokines

Current data analysis so far has revealed a number of subsets and cytokines clearly linked to COVID-19 but the interaction of these components as well as the underlying pathways appear to be very complex and under-appreciated. To obtain a comprehensive overview of the interplay of these key players, we performed Bayesian network analysis using the complete sets of the mass cytometry data of the 327 cell subsets as well as the corresponding bead array measurements of the 13 cytokines (Figure 7 and Table S3). In order to separate the immune signatures of COVID-19 severity from those involved in anti-viral immune response, the fluctuations in these datasets were correlated independently with regard to the time point of sampling during the SARS-CoV-2 infection (Figures 7A and 7B) and the severity score assigned to the respective patient (Figures 7C and 7D). Interactive

viewer for each of the networks is available as online resource (see Materials and Methods: Data and Code Availability)

For the timing of the immune response in the active phase of SARS-CoV-2 infection, the fold change of subset frequency and cytokine levels was determined independently for the median day 9 PIO ("early active"; Figure 7A) and median day 24 PIO ("late active"; Figure 7B). In the early active phase, the strongest correlation was observed for IFNα (Figure 7A). The increase in levels of IFNα inversely correlated with a general decline in the number of NC. Mono including the $CD141^{+}CD11b^{-}$, $CD141^{-}HLA\text{-}DR1^{-}$, $CD45RO^{-}$ and $CD16^{+}CD11b^{-}$ subsets. For these cells, the absolute fold change was between 5 to 8, and the most pronounced reduction observed during the early active phase. The most substantial increase was detected for $CD38^{high}$ $CD45RA^{+}$ pDC and subsets of C. Mono expressing CD169, a marker directly induced by IFNα (compare Figure 6D). Other subsets positively associated with the early phase of infection included several subsets of plasmablasts, activated B memory and Vδ2 T cells. Of these, IgA^{-} plasmabasts positively correlated with IL6, which is also significantly upregulated in the early phase. The increase in plasma IL6 was also associated with a loss of $CD8^{+}$ T cells, MAIT and cDC2. In addition, elevated IP10 was a node associated with a depletion of MAIT and certain B cell subsets (NSM $CD27^{+}CD38^{-}$ and NSM $CD27^{-}CD38^{+}$). However, we did not find any nodal association with Vδ2 T cells, C. Mono and pDC populations to any of the cytokines, while SCF and IL1RA were nonetheless early responders in the blood.

During the late active phase of SARS-CoV-2 infection, the IFNα levels dominating the early phase strongly subsided (Figure 7B). Although the correlation with NC. Mono nearly diminished, Int. and C. Mono strongly expanded in this phase, in particularly for the $CD169^{+}$ subsets with a 8-fold increase in frequency. Next, the correlation with IL6 levels maintained at the late active phase but also two other cytokines, VEGF-A and TNFα, begun to show multiple cellular associations corresponding to significant losses of γδ T, ILC2 and

MAIT cells, while IL6 was a node associated with late increase in LD Neu and Int. Mono, potentially linking these cytokines to the lymphopenia, neutrophilia and monocytosis, which are characteristic of SARS-CoV-2 infection.

A strikingly different picture emerged when the network analysis was carried out in reference to the severity of COVID-19 manifestation. Due to the different nature of the immune response during active infection and convalescence, two independent networks were generated for severity groups I to III ("active"; Figure 7C) and groups IV to VI ("conv."; Figure 7D). The degree of association was determined by a linear correlation of the subset frequencies and cytokine levels in these groups and is expressed by their rho value. Notably during the active phase, the strongest positive correlation was observed for LD Neu and its $CD38^+$, $PD\text{-}L1^+$, IgA^+ and $CD5^+$ subsets (Figure 7C). With the exception of the latter, all of them also positively correlated with HGF, which was also directly associated with disease severity. While an increase in HGF correlated with an increased frequency of LD Neu subsets, it was also associated with a loss of NKT cells, namely of the $CD57^-$ subsets. Although their frequencies were inversely associated with disease severity, this does not necessarily indicate a beneficial effect, as the disappearance of these subsets from the blood may likely be a consequence of their redistribution towards the inflamed tissue. Other subsets, which positively associated with severity are IgA^- plasmablasts and $CD16^+CD11b^-$ C. Mono, possibly pointing to the role of IgG in the COVID-19 pathogenesis. Moreover, plasmablast frequencies directly correlated with IL6 levels, which were also inversely associated with cDC2. Similar to pDC and Vδ2 T cells, their frequencies in the blood also inversely correlated with disease severity.

The direct association of the LD Neu subsets with severity was also observed during convalescence, and no significant negative correlation was detected for any of the immune subsets (Figure 7D). Positive correlations were found for IgA^+ NC. Mono, several $CD8^+$ TEM subsets, as well as $CD38^+$, $CD5^+$, IgA^+ and $PD\text{-}L1^+$ LD Neu. Of the cytokines, VEGF-A, HGF and TNFα correlated directly with severity, while fewer interactions between cytokines and

cell subsets were detected. At least during convalescence, the increase in TNFα but not HGF was positively associated with IgA^+ LD Neu and $PD\text{-}L1^+$ LD Neu subsets (Cross et al., 2008). Additionally, elevated VEGF-A levels strongly associated with enriched $HLA\text{-}DR^+CD38^+CD8^+$ T cells(Voron et al., 2015), which are also directly associated with severity. While especially the early response against SARS-CoV-2 seems to be dominated by IFNα- and IL6-driven immune responses (Figures 7A and 7B), network analysis did not provide any evidence that the pathways and cellular components activated by these cytokines have a major impact on the severity of the disease in either the active phase of infection (Figure 7C) or during convalescence (Figure 7D).

Discussion

COVID-19 is triggered by viral infection whose pathology is mainly caused by collateral or even autoimmune-like damage inflicted by a hyperactivated immune system. By analyzing the blood samples of 77 hospitalized COVID-19 patients by mass cytometry and cytokine bead arrays, we attempted to delineate the key factors driving the immune pathology of COVID-19 from the genuine defense against SARS-CoV-2. To achieve this, we segregated the PBMCs into 327 distinct immune cell subsets and determined the plasma levels of 28 different chemokines and cytokines. The data were stratified with regard to different phases of the viral infection and correlated with the severity score defined by the clinical state of the patients. This generates a comprehensive data resource to analyze the immune response triggered by the SARS-CoV-2 infection in an integrated and interactive way.

A simplified timeline could be established by the breakdown of the infection into four phases (early/late active and early/late convalescence). The time point of the given cell subset was assessed by comparing their relative frequencies in these phases, and their contribution to severity was quantified by the rho^2 parameter of the disease score correlation (Figure S8). Based on this, we propose the following immune progression: infection with SARS-CoV-2 leads to early IFN-α production, as evidenced by an early upregulation of CD169 on monocytes. This drives the disappearance of NC. Mono from the blood, which together with Vδ2 T, cDC2, pDC, NKT, $CD8^+$ MAIT and $CD8^+$ T cells appear to be recruited to the inflamed tissues. In parallel, during this early active phase (median days PIO: 9) there is also an expansion of activated memory B cells and importantly, antibody-producing plasmablasts. The plasmablast frequency remains high during the late active phase, a process associated with elevated levels of the proinflammatory cytokines IL6, IP10 and TNFα.

The late active phase (median days PIO: 20) is also characterized by an expansion of C. Mono, which likely differentiates into Int. and NC. Mono. The relative fraction of Int.

Mono remained high during convalescence, above healthy controls even at the late convalescent phase (median days PIO: 39). In comparison, NC. Mono frequency was the highest during convalescence (Figure 3A). The same applies for $CD8^+$ TEM cells, in particular for the $HLADR^+CD38^+$ subset, which has been found to be enriched in lungs of deceased COVID-19 patients (Xu et al., 2020). Notably, major changes in the frequency of NK subsets were only observed during convalescence, suggestive of a minor role during the early phase of infection.

Disease resolution and convalescence usually result in the normalization of most cell subsets. Notably, the late convalescent subsets, including hyperactivated $HLADR^+CD38^+$ $CD8^+$ T cells, senescent $CD57^+$ $CD4^+$ T cells, Treg TCM/TEM, activated $ICOS^+/CD38^+$ T_{FH}, NC. Mono, Vδ2 TCM/TEM, lymph node homing $CCR6^+$ CSM B cells, NSM B cells and IL12-producing $CD5^-$ cDC2 cells, persistently failed to recover to healthy levels, and may contribute to the lingering symptoms associated to post-infection aberrations (Figure 3B). Further studies would be needed to determine if alterations to these immune subsets contribute to the long-term effects observed in some patients after recovery from severe disease (Weerahandi et al., 2020).

While the involvement of immune cell subsets in anti-viral defense can be heterogeneous, a clearer picture emerges when considering specific immunotypes related to COVID-19 severity. Among the frequencies of subsets such as NC. Mono, Vδ2 T, cDC2, pDC, $CD57^-$ NKT, $CD8^+$ MAIT, and $CD8^+$ T cells showing depletion or enrichment for plasmablasts during infection (Figures S3-S7), the most dramatic severity association was observed for LD Neu (Figure S3). Although LD Neu is virtually absent in the blood of healthy donors, extreme levels were often detected in the blood in the most severe group of patients requiring supplemental O_2 and/or ICU. Due to their high density, neutrophils are not expected to be part of the PBMC fraction. However, processes like neutrophil degranulation can reduce the cell density, which allows them to ‘contaminate’ the lymphocyte/monocyte fraction during Ficoll separation (Hacbarth and Kajdacsy-Balla, 1986). As degranulation is

an integral part of neutrophil biology, the number of LD Neu in the blood may indicate the extent of ongoing neutrophil responses. Previous studies have reported increased numbers of activated neutrophils inside the inflamed lung tissue (Barnes et al., 2020; Fox et al., 2020; Wang et al., 2020; Yao et al., 2020) as well as elevated levels of immature neutrophils in the blood circulation of COVID-19 patients (Carissimo et al., 2020). This is in line with another recent study showing the presence of neutrophil extracellular traps (NETs) in the lungs of deceased COVID-19 patients (Radermecker et al., 2020). Notably, LD Neu seems to have a heightened capacity to release NETs (Yu and Su, 2013). In fact, LD Neu and NET formation have been reported in a number of autoimmune diseases, such as antiphospholipid syndrome (Mauracher et al., 2020), systemic lupus erythematosus(Van Den Hoogen et al., 2020), and anti-neutrophil cytoplasm autoantibody vasculitis (Ui Mhaonaigh et al., 2019), potentially consistent with autoimmune-like features of COVID-19 pathology (Woodruff et al., 2020).

As monocytes has been implicated in COVID-19 pathology (Bedin et al., 2020; Guo et al., 2020; Silvin et al., 2020; Zhou et al., 2020), we further characterized the monocyte population into about 90 different subsets. As expected, IFNα is linked to the induction of $CD169^{+}$ C. Mono during the early active phase as well as the expansion of $CD16^{hi}$ monocyte populations, however we failed to observe any significant association with disease severity. The only exception may be the expansion of $CD16^{+}CD11b^{-}$ C. Mono (Figure 7C) during the active phase and possibly IgA^{+} NC. Mono during convalescence (Figure 7D). Here, we could neither confirm the protective effect of $CD169^{+}$ C. Mono nor the increase of $CD141^{+}HLADR^{-}$ C Mono in severe cases as reported by Hadjadj et al. (Hadjadj et al., 2020). A possible explanation for the discrepancy may be the difference in the timeline of sample taking or in the respective definition of severity; in Hadjadi's study, 'mild' cases were essentially asymptomatic but all of our patients were hospitalized.

Lastly, our study goes a step further by directly linking the neutrophil-specific immune response to the pathology of COVID-19. One of the most striking results is the strong

association between LD Neu frequency and HGF plasma levels. Both factors are directly associated with COVID-19 severity, suggesting that the cytokine may also play a key role in the pathology. The associative nature of this study however does not allow us to draw direct causal conclusions. Furthermore, the source of HGF is still controversial. While the bulk of HGF seems to be released by mesenchymal cells, neutrophils may still play an important role by acting as a source of matured HGF (Ohnishi et al., 2006; Small and Lung, 2006; Wislez et al., 2003). HGF typically acts as anti-inflammatory and supports wound healing. For instance, mesenchymal stem cells have been shown to alleviate acute lung injury via the paracrine secretion of HGF (Lu et al., 2019). HGF and its receptor c-MET also play a crucial role in various cancer where the neutrophil/HGF axis seems to mediate tumor growth by eliciting immune-suppression (Glodde et al., 2017). However, depending on differentiation and tissue environment, neutrophils can exert both pro- and anti-inflammatory effects (Rosales, 2018). An earlier *in vitro* study even suggested that HGF stimulates neutrophil degranulation (Kowanko et al., 1993). It is therefore likely that the presence of HGF in severe COVID-19 may also promote the release of NETs (Radermecker et al., 2020). It may thus be worth to evaluate existing HGF/c-MET drugs with regard to their ability to prevent or stop deteriorating COVID-19 symptoms.

In summary, while the cellular and molecular interactions underlying COVID-19 are very complex, we have identified some new candidates for potential treatment interventions. Here, the HGF/LD Neu axis may represent a promising new lead for direct interventions, and future studies have to show if HGF is actually a better pharmacological target than IFNα and IL6. The trials with IL6 inhibitors have already failed and there is acute demand for effective treatments. In support of this hunt, this study generates a database that could be used as a crucial resource to evaluate the pathways and to validate, identify or exclude candidate targets that could help to control the ongoing pandemic.

Materials and Methods

Study design, sample size and participants

For this study, 77 COVID-19 patients and 10 healthy donors were recruited. Enrollment of COVID-19 patients was via PROTECT, a Singapore COVID-19 cohort study among seven public health institutions. Healthy individuals were recruited under a Singapore Immunology Network study entitled, “Study of blood cell subsets and their products in models of infection, inflammation and immune regulation”. Both studies had received prior approval from their respective institutional review boards (IRBs). All individuals involved in this study were over the age of 21, comprising 66 males and 21 females. Additional demographic details can be found in Table S1.

Sample collection

Blood from healthy adult donors and COVID-19 patients were collected in BD Vacutainer CPT Tubes and processed according to manufacturer’s instructions to obtain the PBMC and plasma fractions. Isolated PBMCs were then used for mass cytometry staining after two washes with 1X phosphate buffer saline (PBS).

Cytometry by time-of-flight (CyTOF) sample processing and data acquisition

Freshly isolated ficoll-density centrifuged PBMCs were plated at 0.5 – 1 x 10^6 in a 96-well V bottom plates and stained for viability with 100 µL of 66 µM of cisplatin (Sigma-Aldrich) for 5 minutes on ice. Cells were then washed with staining buffer (4% v/v fetal bovine serum, 0.05% v/v sodium azide in 1X PBS) and stained with anti-γδTCR-PE and anti-Vδ1-FITC in 50 µL reaction volume for 15 minutes at room temperature. Cells were washed with staining buffer and then stained with 50 µL of metal isotope-labeled surface antibodies on ice. After 20 minutes, cells were washed with staining buffer, followed by PBS, and fixed in 4% v/v paraformaldehyde (PFA, Electron Microscopy Sciences) at 4°C overnight. On the following

day, cells were incubated in staining buffer for 5 minutes. Cellular DNA was labeled at room temperature with 170 nM iridium intercalator (Fluidigm) in 2% v/v PFA/PBS. After 20 minutes, cells were washed twice with staining buffer.

Prior to CyTOF acquisition, cells were washed twice with water before final re-suspension in water. Cells were enumerated, filtered and diluted to a final concentration of 0.6 x 10^6 cells/mL. EQ Four Element Calibration Beads (Fluidigm) were added to the samples at a final concentration of 2% v/v prior to acquisition. Samples were acquired on a Helios Mass Cytometer (Fluidigm) at an event rate of < 500 events per second. After CyTOF acquisition, data were exported in flow-cytometry (FCS) format, normalized to 300,000 PBMCs and events with parameters having zero values were randomized using a uniform distribution of values between minus-one and zero. Subsequently, manual gating was performed to exclude residual beads, debris and dead cells.

Gating strategy for CyTOF

We have designed a 40-plex antibodies panel for mass cytometry and performed non-supervised Uniform Manifold Approximation and Projection (UMAP) or Triplet-constraint (TriMAP) dimensionality reduction for larger dataset embedding of ficoll-density centrifuged PBMCs obtained from both COVID-19 active and convalescent patients (Amid and Warmuth, 2019; McInnes et al., 2018). Iterative manual and UMAP clustering identified populations of T cells, B cells, monocytes, NK, DC, ILCs, basophil as well as the LD neutrophils based on their cell surface expression markers to generate 327 different immune cell subpopulations.

Multiplex microbead-based Luminex immunoassays

Plasma samples were treated by solvent/detergent based on Triton™ X-100 (1%) for virus inactivation (Darnell and Taylor, 2006). Immune mediator levels in COVID-19 patient plasma across different active and convalescent groups were measured with 24-plex Human

ProcartaPlex™ (ThermoFisher Scientific). The kit analyte detection panel included brain-derived neurotrophic factor (BDNF), beta-nerve growth factor (bNGF), hepatocyte growth factor (HGF), monocyte chemoattractant protein (MCP) 1, macrophage inflammatory protein (MIP) 1α, MIP1β, RANTES (regulated on activation, normal T cell expressed and secreted), stromal cell-derived factor 1 (SDF1α), interferon (IFN) gamma-induced protein 10 (IP10), IFNγ, interleukin (IL) IL1β, IL1RA, IL2, IL5, IL6, IL7, IL18, IL12p70, leukemia inhibitory factor (LIF), stem cell factor (SCF), tumor necrosis factor (TNFα), vascular endothelial growth factor A (VEGF-A), platelet derived growth factor (PDGF-BB), and placental growth factor (PLGF1).

Plasma from COVID-19 patients, healthy controls, as well as standards were incubated with fluorescent-coded magnetic beads pre-coated with respective antibodies in a black 96-well clear-bottom plate overnight at 4˚C. After incubation, plates were washed 5 times with wash buffer (PBS with 1% v/v bovine serum albumin (Capricorn Scientific) and 0.05% v/v Tween-20 (Promega)). Sample-antibody-bead complexes were incubated with biotinylated detection antibodies for 1 hour and washed 5 times with wash buffer. Subsequently, Streptavidin-PE was added and incubated for another 30 minutes. Plates were washed 5 times again, before sample-antibody-bead complexes were re-suspended in sheath fluid for acquisition on the FLEXMAP® 3D (Luminex) using xPONENT® 4.0 (Luminex) software. Data analysis was done on Bio-Plex Manager™ 6.1.1 (Bio-Rad). Standard curves were generated with a 5-PL (5-parameter logistic) algorithm, reporting values for both mean florescence intensity (MFI) and concentration data.

Internal control samples were included in each plate to remove any potential plate effects. Readouts of these samples were then used to normalize the assayed plates. A correction factor was obtained from the median concentration values observed across the multiple assay plates and this correction factor was then used to normalize all the samples. The concentrations were logarithmically transformed to ensure normality. Analytes that were not

586 detectable in patient samples were assigned the value of logarithmic transformation of the
587 Limit of Quantification (LOQ).

588

589 **Multiplex microbead-based Quanterix immunoassays**

590 Plasma immune mediator levels in selected active and convalescence phase of COVID-19
591 patients were measured using SIMOA Cytokine 3-Plex B (C3PB) assay kit (Quanterix) and
592 SIMOA IFN-a assay kit (Quanterix). C3PB kit analyte detection included interleukin (IL) IL6,
593 IL17A and tumor necrosis factor α (TNFα).
594 Standards and plasma from COVID-19 patients and healthy controls were pre-diluted in a
595 96-well plate before loading into the Simoa® HD-1 Analyzer (Quanterix) for data acquisition.
596 Reagents from the C3PB and IFNα assay kits were prepared according to the kit manual
597 and loaded into the analyzer. Fully automated data acquisition was done on Simoa® HD-1
598 Analyzer (Quanterix). Standard curves were generated with a 4-PL (4-parameter logistic)
599 algorithm, reporting values for concentration data.

600

601 **Quantification and Statistical Analysis**

602 Active and convalescence phase samples were defined by PCR positivity and serve as time
603 based clinical end points. Active phase samples were further divided into early (PIO <= 14
604 days) and late (PIO > 14 days). Convalescence phase samples were also further divided
605 into early (PIO <= 28 days) and late (PIO > 28 days). These provide a more granular time
606 based clinical end points.

607 Severity based clinical end points were defined for active and convalescence phase samples
608 separately. Three severity groups were defined for each phase consisting of symptomatic
609 patients, patients requiring oxygen supplementation and patients requiring oxygen
610 supplementation and awarded into intensive care unit as shown in Figure 1A.

Mass cytometry and cytokine measurements were associated to the clinical end points (time based as well as severity based) using Kruskal-Wallis tests followed by Dunn's post hoc tests. Correlations between mass cytometry and cytokine measurements were done using Spearman Rank correlations. In the event that multiple samples from the same patient was available for same time period, the earliest of the samples were used for analyses to ensure that all samples used in the analyses are distinct. Multiple testing correction was done using the method of Benjamini and Hochberg. P values less than 0.05 were deemed to be significant. All statistical tests were two-sided (when appropriate) unless otherwise indicated. Statistical analyses were done using the R statistical language version 3.6.2. All statistical details are provided in the interactive viewers provided at https://data.mendeley.com/datasets/467s57xj8s/draft?a=15341765-e712-4eec-8107-a1d9c8da331a

Overviews of the mass cytometry immune cell subpopulations were generated using UMAP in R version 3.6.2 using the uwot package. Heat maps were generated in R version 3.6.2 using the CompexHeatmap package. Graphs of the significant associations were generated in R version 3.6.2 using the iGraph package and visualized in Cytoscape version 3.8.0. Additional visualizations were done in TIBCO Spotfire.

Data and Code Availability

Data generated and/or analyzed during this study are available in the following public repositories and also at https://data.mendeley.com/datasets/467s57xj8s/draft?a=15341765-e712-4eec-8107-a1d9c8da331a.

An interactive viewer of the mass cytometry data associations with clinical endpoints (Figures 2A, 3, 5A and 5B and S2) are available at https://www.dropbox.com/s/wz93vwn2vvjsjry/cytof_sample_group_association_results_paper_vis_covid19_cytof_results_viewer.html?dl=1

637 An interactive viewer of the cytokine data associations with clinical endpoints (Figures 6A
638 and 6B) are available at
639 https://www.dropbox.com/s/4v107l3b65h5qfh/luminex_sample_group_association_results_vi
640 s_covid19_cytof_results_viewer.html?dl=1

641 The mass cytometry, cytokine and clinical data is available as an Excel file at
642 https://www.dropbox.com/s/yd2spn3lholhuv3/all_cytof_multimodal_data_paper.xlsx?dl=1

643 An interactive viewer of interaction network in Figure 7A is available at
644 https://www.dropbox.com/s/zm7a4s6nqelfnso/network_data_early_active_late_con_all_subs
645 et_percent_only_vis_bivariatetests.html?dl=1

646 An interactive viewer of interaction network in Figure 7B is available at
647 https://www.dropbox.com/s/yt8sf6uwhtte55y/network_data_late_active_late_con_all_subset
648 _percent_only_vis_bivariatetests.html?dl=1

649 An interactive viewer of interaction network in Figure 7C is available at
650 https://www.dropbox.com/s/50tfhif6eqz3uoa/network_data_active_all_subset_percent_only_i
651 cu_regression_vis_bivariatetests.html?dl=1

652 An interactive viewer of interaction network in Figure 7D is available at
653 https://www.dropbox.com/s/q43bz8s294bwobu/network_data_con_all_subset_percent_only_
654 icu_regression_vis_bivariatetests.html?dl=1

655 An interactive viewer of cytokine data correlation with mass cytometry data at active phase
656 (Figures 6C and 6D) is available at
657 https://www.dropbox.com/s/6y6bo7zl40qlm26/luminex_correlation_analysis_active_convales
658 cence_group_active_results_vis_stats_results_viewer.html?dl=1

659 An interactive viewer of cytokine data correlation with mass cytometry data at convalescence
660 phase (Figure 6C) is available at

661 https://www.dropbox.com/s/2h0awk6l4rgzmn9/luminex_correlation_analysis_active_convale

662 scence_group_convalescence_results_vis_stats_results_viewer.html?dl=1

Acknowledgements:

This study was funded by grants from Singapore's National Medical Research Council (NMRC)'s COVID-19 Research Fund (grant numbers COVID19RF-001, COVID19RF-004, and COVID19RF-007), as well as the Biomedical Research Council COVID-19 Fund (grant number H20/04/g1/006) and the A*ccelerate GAP Fund (grant number ACCL/19-GAP064-R20H-H) from the Agency of Science, Technology, and Research, Singapore. We thank Etienne Raimondeau from LaPipette for the design of figure S8. We thank Mark I-Cheng Chen from the National University of Singapore and National University Health System for his support and patient cohort. We thank all clinical and nursing staff who provided medical care to the patients, staff at the Communicable Diseases Division of the Ministry of Health, Singapore, who contributed to the outbreak response and contact tracing, and staff at the Singapore Infectious Disease Clinical Research Network and Infectious Disease Research and Training Office of the National Centre for Infectious Diseases for coordinating patient recruitment.

Author Contributions:

Conceptualization: J.L., P.K.J., L.F.P.N., B.L., O.R.; Methodology: J.L., K.W.W.T., C.Y.L., K.P.T., G.C., Y.H.C., C.M.P., C.Y-P.L., S.-W.F., N.K.-W.Y., R.S.-L.C., S.N.A., Z.W.C., M.Z.T., A.T.-R., N.L.F., W.H.; Software: K.D., B.L.; Validation: J.L., P.K.J.; Formal Analysis: J.L., P.K.J., L.W.W., K.D., B.L.; O.R.; Resources: M.I.-C.C., S.-Y.T., L.Y.A.C., S.K., T.S.-Y., D.C.L., Y.-S.L., S.W.X.O., B.E.Y.; Data Curation: K.D., B.L.; Writing – Original Draft: J.L., P.K.J, L.W.W., B.L., O.R.; Writing – Review & Editing: J.L., P.K.J., L.W.W., B.L., O.R.; Visualization: J.L., P.K.J., L.W.W., B.L., O.R.; Supervision: L.R., L.F.P.N., O.R.; Project Administration: L.F.P.N., O.R.; Funding Acquisition: L.F.P.N.

Competing Interests:

The authors declare no competing interests

688 **Figures:**

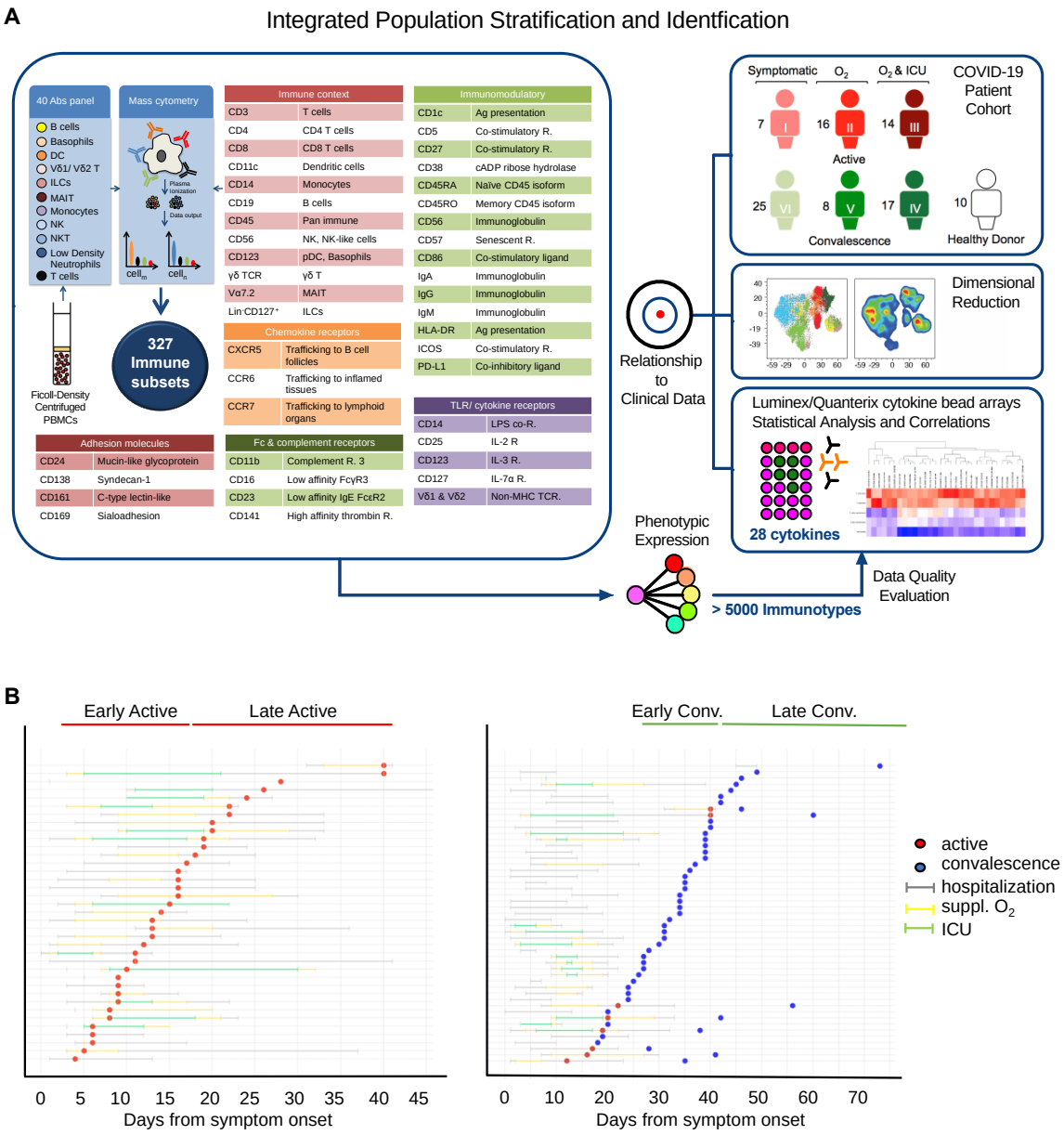

689

690 **Figure 1.** Study design and clinical characteristics of the cohort. (A) Schematic showing the
691 pipeline for sample acquisition and analysis. A list of the antibody targets is presented. (B)
692 Timelines for individual COVID-19 cases, indicating points of sample collection and any
693 clinically pertinent detail e.g. duration of hospitalization, oxygen supplementation and
694 admission to the intensive care unit (ICU).

695

696

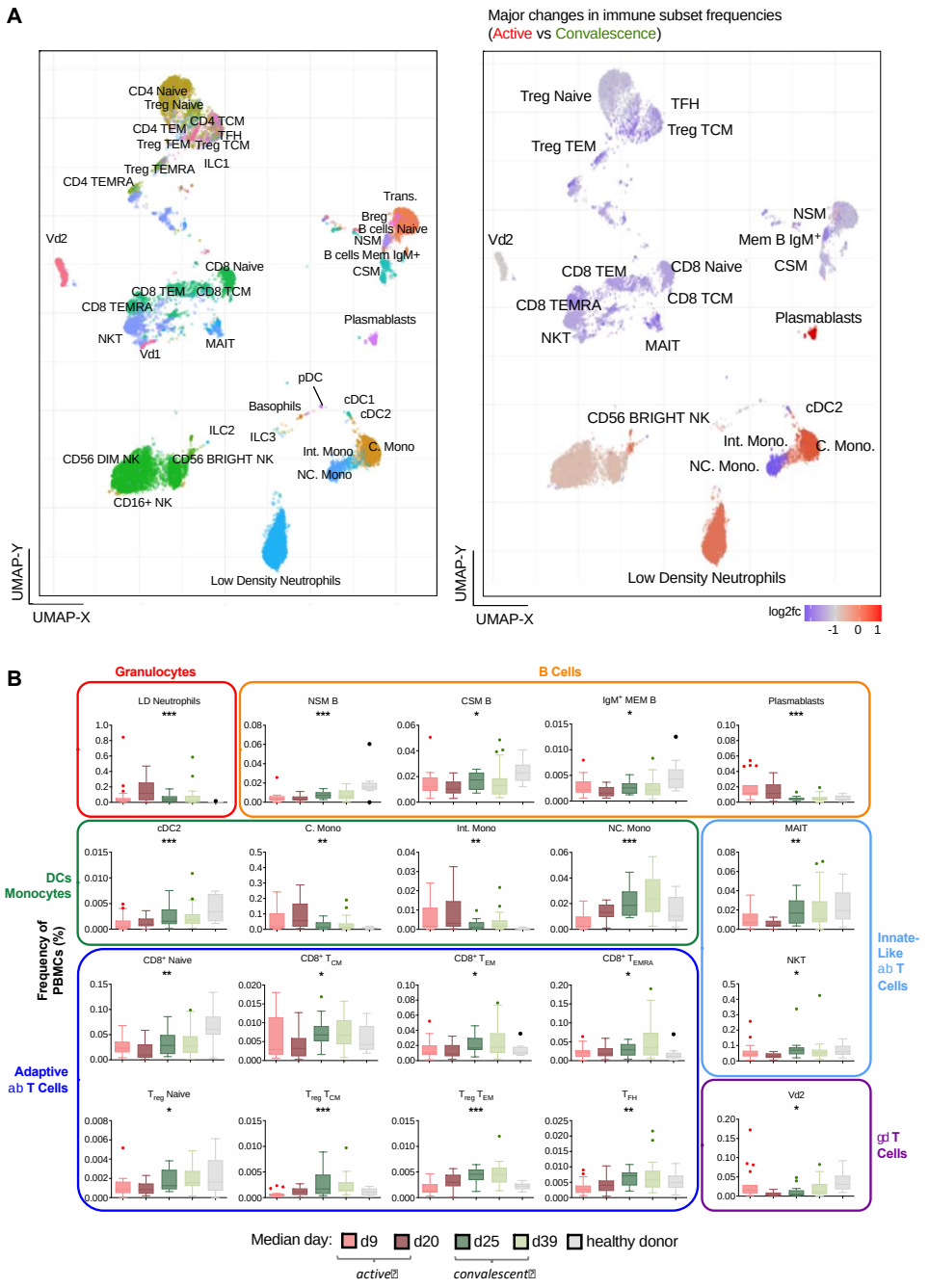

Figure 2. Frequency changes in 38 basic immune cell populations with SARS-CoV-2 infection. (A) Uniform Manifold Approximation and Projection (UMAP) plots of 38 main immune cell populations detected by mass cytometry (left). Right: heat map representation of fold changes in the detected populations during active infection relative to convalescence, with color-coding done on a $\log_2$ scale. (B) Frequency-time plots of immune cell populations of interest over the course of disease.

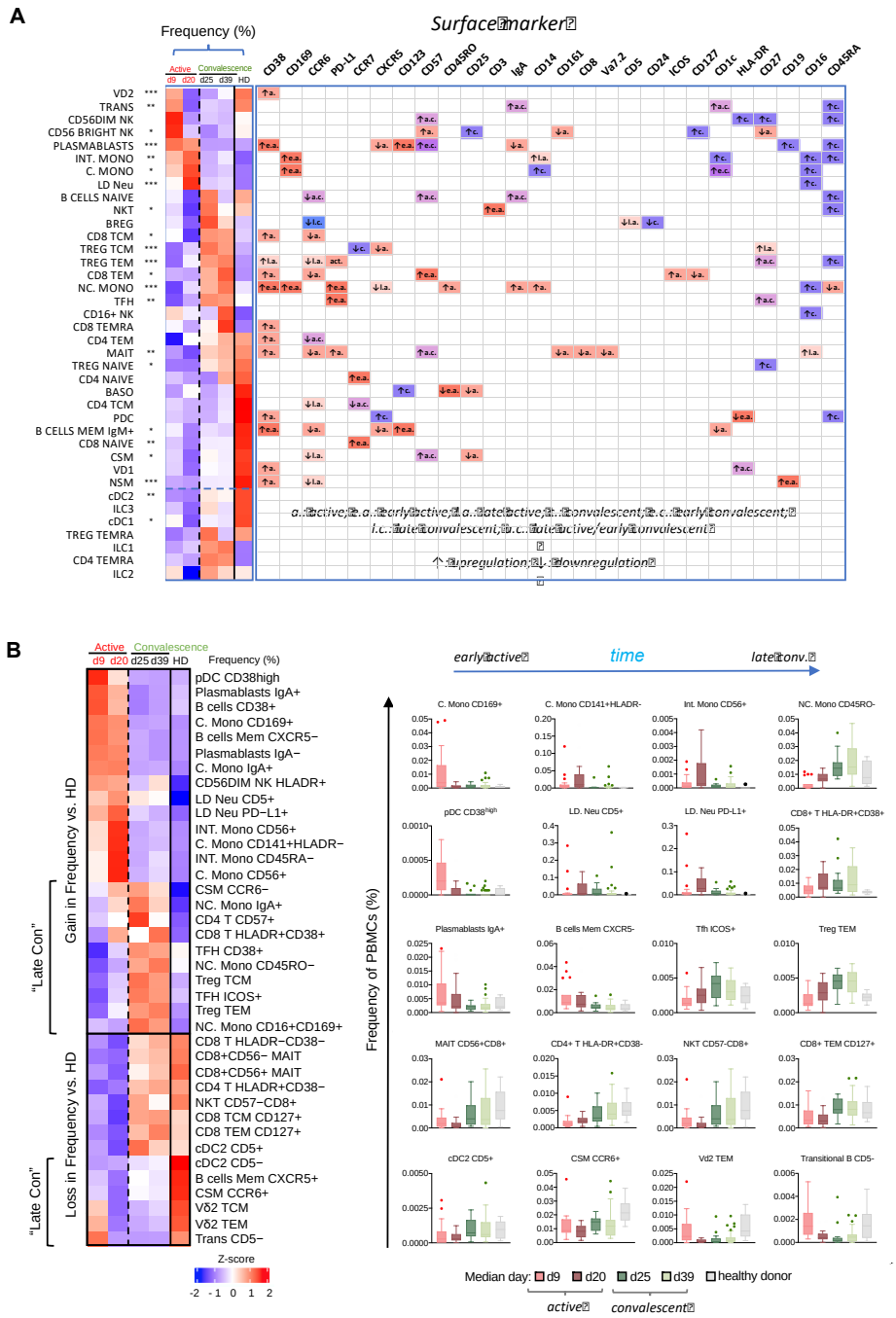

Figure 3. Temporal changes in frequencies and surface marker expression profiles of various immunotypes during active and convalescent COVID-19. (A) Left: heat map representation of the frequencies of all 38 basic immune cell populations as a function of days post illness onset (PIO) – d9 (early active; median: 9 days PIO), d20 (late active; median: 20 days PIO), d25 (early convalescence; median: 25 days PIO), d39 (late convalescence; median: 39 days PIO). Asterisks indicate statistical significance - *, p<0.05; **, p<0.01; ***, p<0.001 (one-way ANOVA of all disease phases and healthy controls). Right:

713 up- or down-regulation of indicated surface markers for the 38 main immune cell populations
714 as a function of disease phase. (B) Left: heat map representation of the frequencies of the
715 top 38 immunotypes as a function of disease phase. Right: Box-and-whiskers plots of select
716 immunotypes showing the frequency-time relationships, with mean and IQR indicated. “Late
717 Con” refers to a group of immune subsets, which fail to recover to healthy levels even in late
718 convalescence as post-infection aberrations.

719

720

721

722

723

724

725

726

727

728

729

730

731

732

733

734

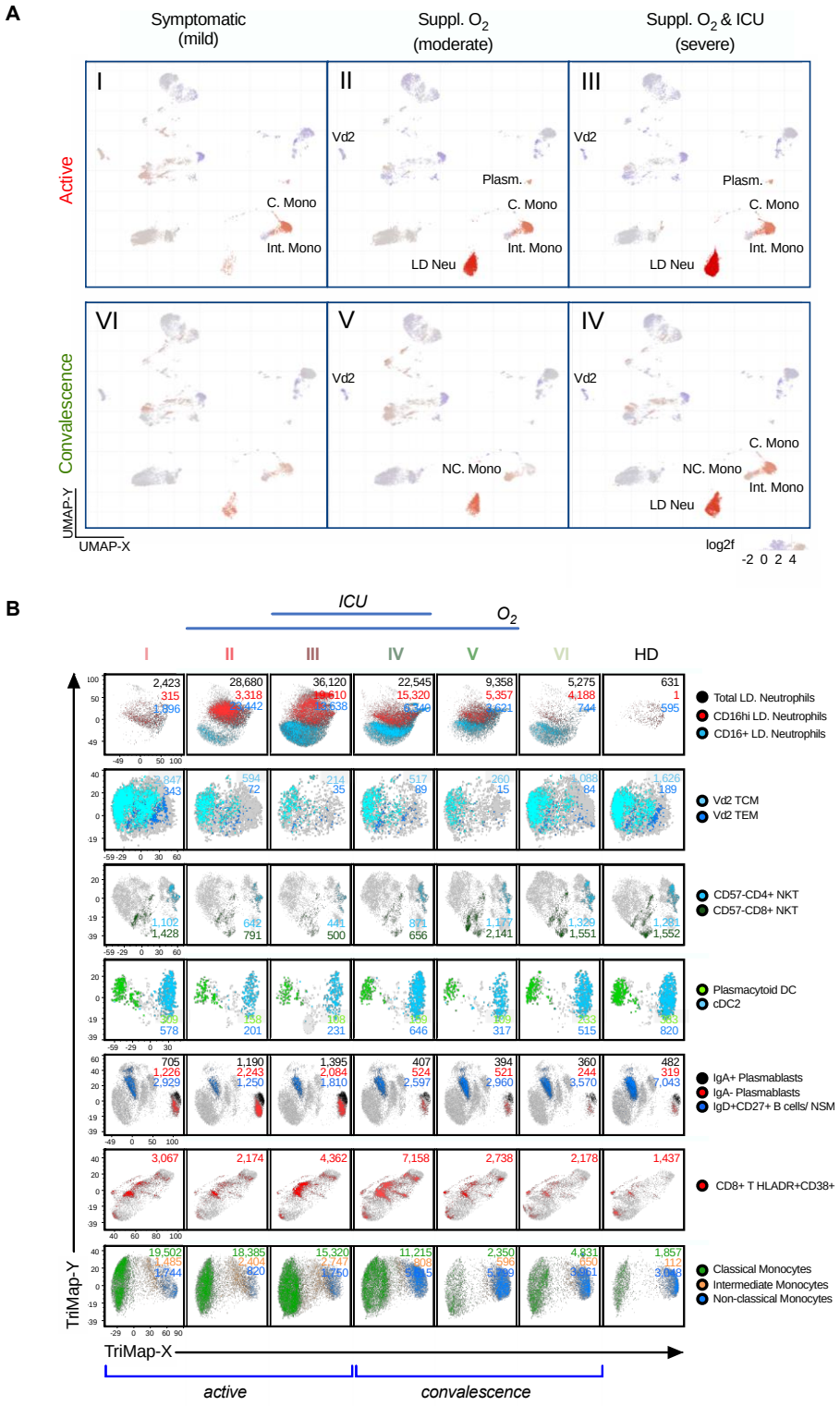

Figure 4. Alterations of immunotypes associated with the six-group disease severity states. (A) Distribution of 38 immune cell subsets among group I active mild symptomatic, group II active suppl. O_2 group III active suppl. O_2 ICU, group IV convalescent suppl. O_2 ICU, group V convalescent Suppl. O_2 and group VI convalescent mild symptomatic using UMAP clustering.

Color indicates the log2 fold change in the frequency against healthy donors. (B) TriMap clustering of PD-L1^{+} LD Neu, Vδ2 TCM, Vδ2 TEM, pan-CD57^{-} NKT, pDC, cDC2, IgA$^{+/-}$ plasmablasts, IgD^{+}CD27^{+} NSM, HLA-DR^{+}CD38^{+} CD8 T cells, C. Mono, Int. Mono and NC. Mono among 6 groups of SAR-CoV-2 patients and healthy donors (HD). The absolute number shown for the immune cells has been normalized per 300,000 PBMCs and thus reflects its frequency.

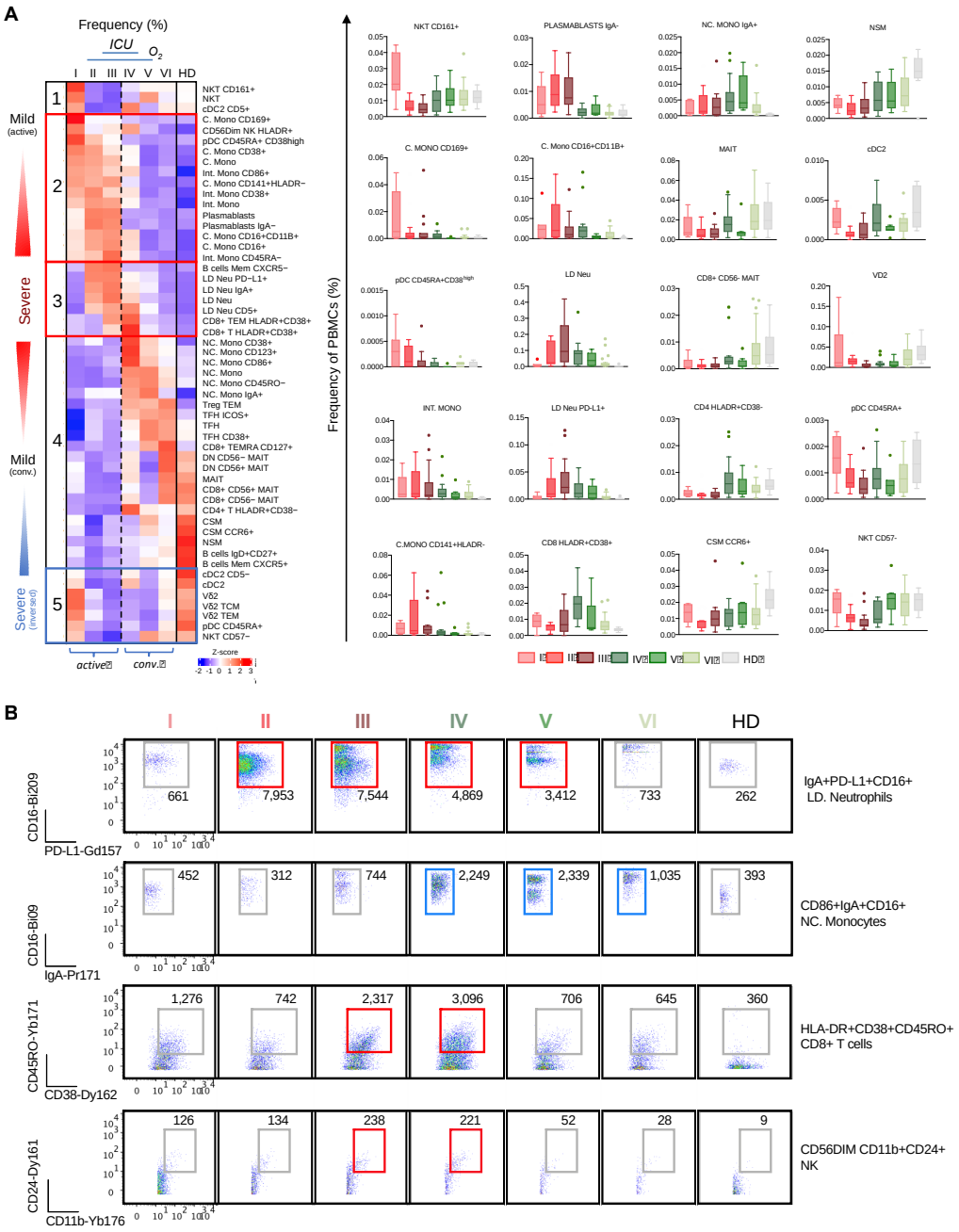

762

763 **Figure 5.** Association of immune cell types and immunotypes with disease severity. (A) Left:
764 Heat map representation of frequencies of 53 immune cell populations with mild active,
765 severe, and mild convalescence among the 6 group severity stratifications and divided into
766 five clusters. Right: Box-and-whiskers plots showing means and IQR increased and reduced
767 frequency of immune cell pollutions with disease severity. (B) Scatterplots of subsets of IgA^+
768 LD Neu, $CD86^+$ NC. Mono, HLA-DR^+ $CD8^+$ T and $C56^{Dim}$ NK cells with each cell population
769 additionally showing co-expression of CD16, PD-L1, IgA, CD45RO, CD38, CD24 and CD11b

770 frequencies. The absolute number shown for the gated immune cells has been normalized
771 per 300,000 PBMCs and thus reflects its frequency.

772

773

774

775

776

777

778

779

780

781

782

783

784

785

786

787

788

789

790

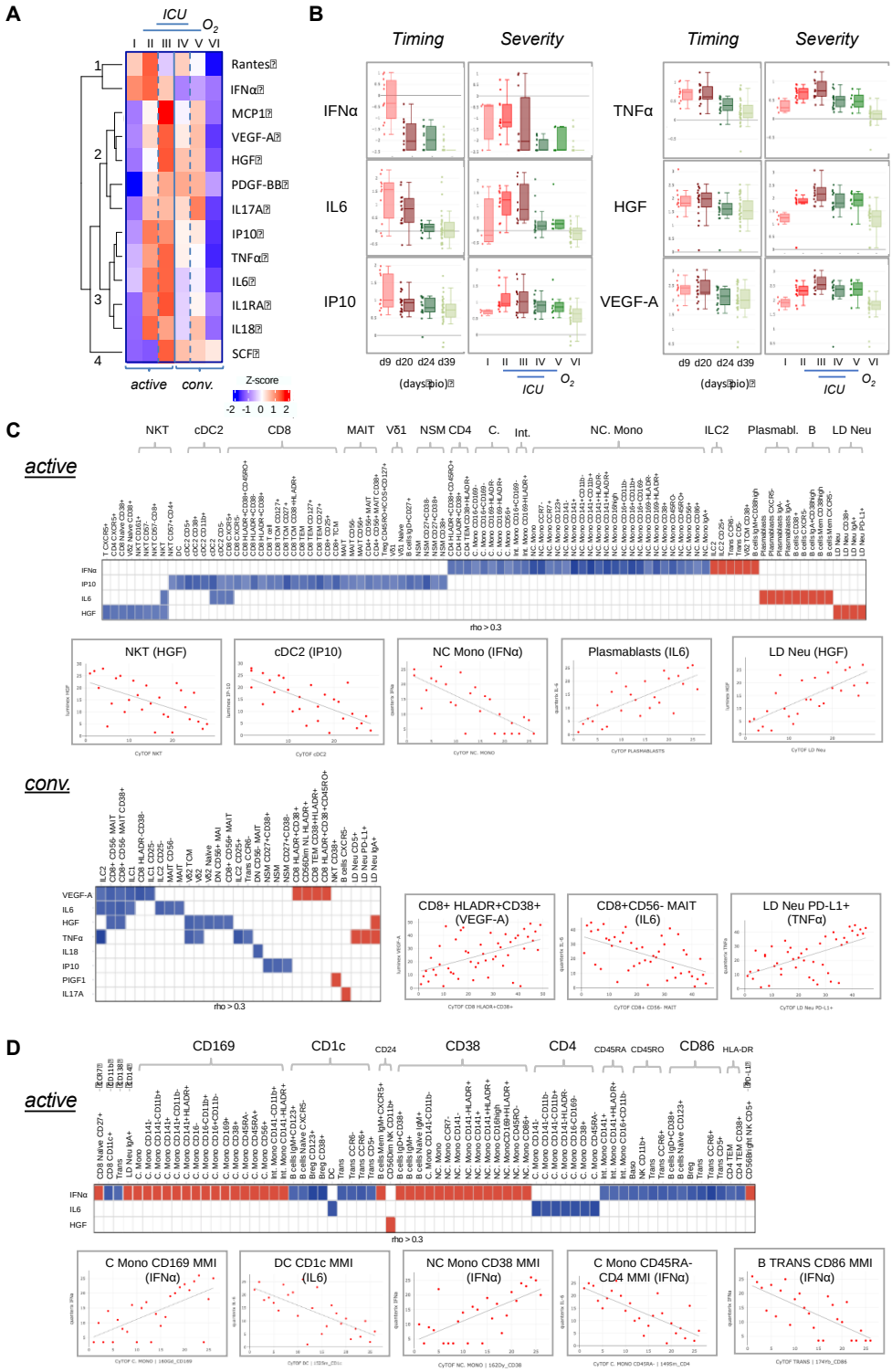

Figure 6. Characterization of cytokines in COVID-19 patients. (A) Changes in cytokine levels among COVID-19 patients based on timing and severity. The heatmap shows the z-scores of the mean logarithmically transformed concentration of the 13 cytokines (of a total of 28) showing significant differences between any of the 6 severity groups. The z-scores are

colored in red for positive values and in blue for negative values. The cytokines are clustered using hierarchical clustering using Euclidean distances into four clusters, which are labeled 1 to 4 in the figure. (B) Box plots of selected cytokines showing differences in timing and/or severity. The timing (left panels) refers to the plasma cytokine levels detected on the respective day post illness onset (PIO), the severity (right panels) to the levels detected in the 6 severity groups. Red colors refer to samples from the active phase, green to convalescence phase. An interactive viewer is available in the online content: data availability section. (C) Associations between cytokine level and cell frequency during active and convalescent phase. The heatmap displays the strength of the association indicated by the correlation coefficient (rho). Color indicated the direction (Red: positive, blue: negative). Only associations abs(rho) > 0.3 and $p < 0.05$ are shown. Selected examples of these correlations are shown in the scatter plots. An interactive viewer is available in the online content: data availability section. (D) Associations between cytokine level and cell surface marker expression during the active phase. The plots are arranged as in Figure 6C except that the correlation was carried out with the MMI values of the various cell surface marker instead of the percentage value of the cell populations.

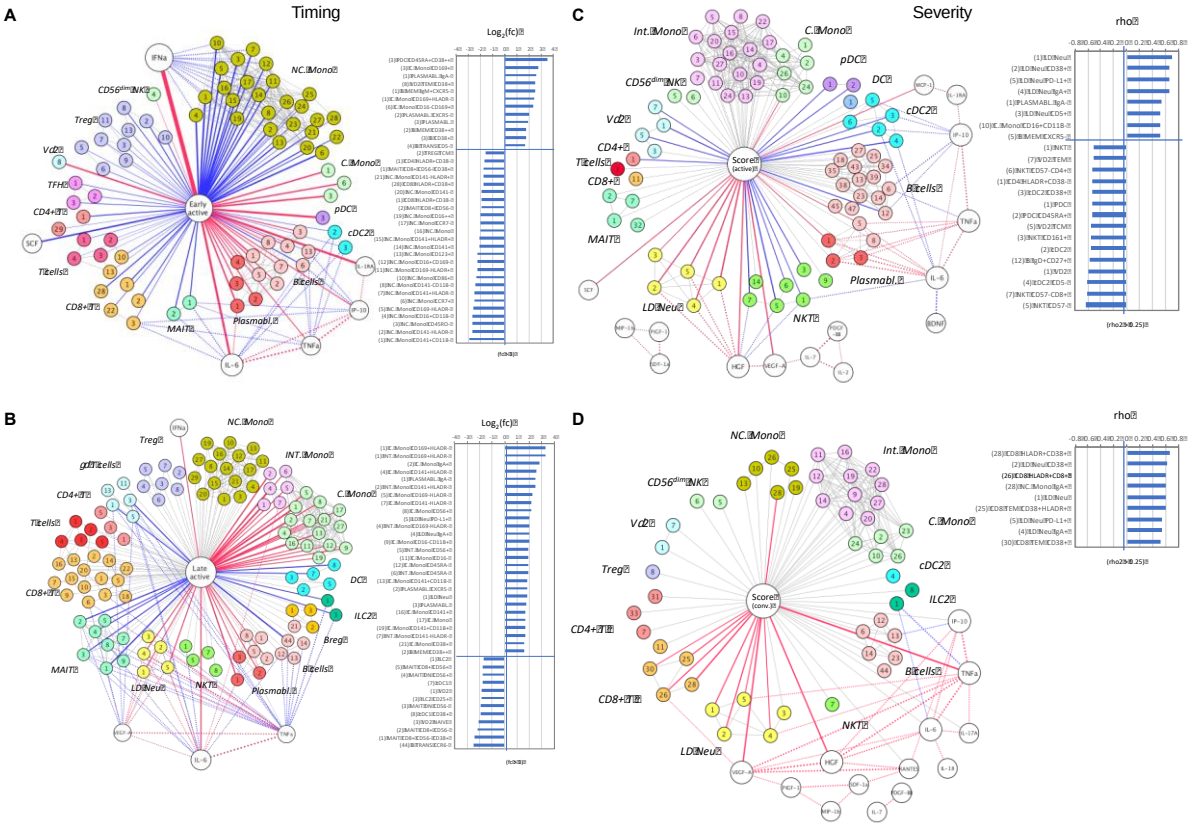

Figure 7. A node-edge interaction network of the cytokine level and immune cellular frequencies in COVID-19 patients. Association are shown with regard to the timing (A, B) and the severity (C, D). Nodes represent either cytokines (white) or immune subsets (colored). The central node represents the “comparison of interest”. The edges represent significant associations between two nodes with the thickness indicating the strength either based on fold change or correlation coefficient (rho). Color indicates the direction (Red: positive, blue: negative), dotted lines indicate associations with cytokines. For the central node, only associations with abs(rho) > 0.3 and $p < 0.05$ are colored and shown as bar charts on the right. For the timing (A, B) these bar charts indicate the fold changes in the early active (A) and late active state (B) in reference to late convalescent state while for the severity (C, D) they represent the correlation coefficient (rho) in reference to the severity groups in the active (C) and convalescent state (D). The number code of the cell subsets is listed in table S3, an interactive network viewer is available in the Materials and Methods: data and code availability subsection and Key Resource Table. $^{++}$ denotes highly stained immunotype.

References

Amid E, Warmuth MK. 2019. TriMap: large-scale dimensionality reduction using triplets. *arXiv*.

Barnes BJ, Adrover JM, Baxter-Stoltzfus A, Borczuk A, Cools-Lartigue J, Crawford JM, Daßler-Plenker J, Guerci P, Huynh C, Knight JS, Loda M, Looney MR, McAllister F, Rayes R, Renaud S, Rousseau S, Salvatore S, Schwartz RE, Spicer JD, Yost CC, Weber A, Zuo Y, Egeblad M. 2020. Targeting potential drivers of COVID-19: Neutrophil extracellular traps. *J Exp Med*. doi:10.1084/jem.20200652

Bedin A-S, Makinson A, Picot M-C, Mennechet F, Malergue F, Pisoni A, Nyiramigisha E, Montagnier L, Bollore K, Debiesse S, Morquin D, Bourgoin P, Veyrenche N, Renault C, Foulongne V, Bret C, Bourdin A, Le Moing V, Van de Perre P, Tuaillon E. 2020. Monocyte CD169 expression as a biomarker in the early diagnosis of COVID-19. *J Infect Dis*. doi:10.1093/infdis/jiaa724

Carissimo G, Xu W, Kwok I, Abdad MY, Chan YH, Fong SW, Puan KJ, Lee CYP, Yeo NKW, Amrun SN, Chee RSL, How W, Chan S, Fan BE, Andiappan AK, Lee B, Rötzschke O, Young BE, Leo YS, Lye DC, Renia L, Ng LG, Larbi A, Ng LF. 2020. Whole blood immunophenotyping uncovers immature neutrophil-to-VD2 T-cell ratio as an early marker for severe COVID-19. *Nat Commun*. doi:10.1038/s41467-020-19080-6

Corman VM, Landt O, Kaiser M, Molenkamp R, Meijer A, Chu DKW, Bleicker T, Brünink S, Schneider J, Schmidt ML, Mulders DGJC, Haagmans BL, Van Der Veer B, Van Den Brink S, Wijsman L, Goderski G, Romette JL, Ellis J, Zambon M, Peiris M, Goossens H, Reusken C, Koopmans MPG, Drosten C. 2020. Detection of 2019 novel coronavirus (2019-nCoV) by real-time RT-PCR. *Eurosurveillance*. doi:10.2807/1560-7917.ES.2020.25.3.2000045

Cross A, Moots RJ, Edwards SW. 2008. The dual effects of TNFα on neutrophil apoptosis are mediated via differential effects on expression of Mcl-1 and Bfl-1. *Blood*. doi:10.1182/blood-2007-05-087833

Darnell MER, Taylor DR. 2006. Evaluation of inactivation methods for severe acute respiratory syndrome coronavirus in noncellular blood products. *Transfusion*. doi:10.1111/j.1537-2995.2006.00976.x

Dong E, Du H, Gardner L. 2020. An interactive web-based dashboard to track COVID-19 in real time. *Lancet Infect Dis* **20**:533–534. doi:10.1016/S1473-3099(20)30120-1

Fox S, Akmatbekov A, Harbert J, Li G, Brown JQ, Vander Heide R. 2020. Pulmonary and Cardiac Pathology in Covid-19: The First Autopsy Series from New Orleans. *Lancet Respir Med*. doi:10.1101/2020.04.06.20050575

Glodde N, Bald T, van den Boorn-Konijnenberg D, Nakamura K, O'Donnell JS, Szczepanski S, Brandes M, Eickhoff S, Das I, Shridhar N, Hinze D, Rogava M, van der Sluis TC, Ruotsalainen JJ, Gaffal E, Landsberg J, Ludwig KU, Wilhelm C, Riek-Burchardt M, Müller AJ, Gebhardt C, Scolyer RA, Long G V., Janzen V, Teng MWL, Kastenmüller W, Mazzone M, Smyth MJ, Tüting T, Hölzel M. 2017. Reactive Neutrophil Responses Dependent on the Receptor Tyrosine Kinase c-MET Limit Cancer Immunotherapy. *Immunity*. doi:10.1016/j.immuni.2017.09.012

Guo C, Li B, Ma H, Wang X, Cai P, Yu Q, Zhu L, Jin L, Jiang C, Fang J, Liu Q, Zong D, Zhang W, Lu Y, Li K, Gao X, Fu B, Liu L, Ma X, Weng J, Wei H, Jin T, Lin J, Qu K. 2020. Single-cell analysis of two severe COVID-19 patients reveals a monocyte-associated and tocilizumab-responding cytokine storm. *Nat Commun*. doi:10.1038/s41467-020-17834-w

884 Hacbarth E, Kajdacsy-Balla A. 1986. Low density neutrophils in patients with systemic lupus
885 erythematosus, rheumatoid arthritis, and acute rheumatic fever. *Arthritis Rheum*.
886 doi:10.1002/art.1780291105

887 Hadjadj J, Yatim N, Barnabei L, Corneau A, Boussier J, Smith N, Péré H, Charbit B, Bondet
888 V, Chenevier-Gobeaux C, Breillat P, Carlier N, Gauzit R, Morbieu C, Pène F, Marin N,
889 Roche N, Szwebel TA, Merkling SH, Treluyer JM, Veyer D, Mouthon L, Blanc C,
890 Tharaux PL, Rozenberg F, Fischer A, Duffy D, Rieux-Laucat F, Kernéis S, Terrier B.
891 2020. Impaired type I interferon activity and inflammatory responses in severe COVID-
892 19 patients. *Science (80-)*. doi:10.1126/science.abc6027

893 Jouan Y, Guillon A, Gonzalez L, Perez Y, Ehrmann S, Ferreira M, Daix T, Jeannet R,
894 Francois B, Dequin P-F, Si-Tahar M, Baranek T, Paget C. 2020. Functional alteration of
895 innate T cells in critically ill Covid-19 patients. *medRxiv* 2020.05.03.20089300.
896 doi:10.1101/2020.05.03.20089300

897 Kowanko IC, Ferrante A, Nakamura T. 1993. Hepatocyte growth factor stimulates neutrophil
898 degranulation but not respiratory burst. *Mediators Inflamm*.
899 doi:10.1155/S0962935193000195

900 Kuri-Cervantes L, Pampena MB, Meng W, Rosenfeld AM, Ittner CAG, Weisman AR,
901 Agyekum RS, Mathew D, Baxter AE, Vella LA, Kuthuru O, Apostolidis SA, Bershaw L,
902 Dougherty J, Greenplate AR, Pattekar A, Kim J, Han N, Gouma S, Weirick ME, Arevalo
903 CP, Bolton MJ, Goodwin EC, Anderson EM, Hensley SE, Jones TK, Mangalmurti NS,
904 Luning Prak ET, Wherry EJ, Meyer NJ, Betts MR. 2020. Comprehensive mapping of
905 immune perturbations associated with severe COVID-19. *Sci Immunol*.
906 doi:10.1126/sciimmunol.abd7114

907 Lu Z, Chang W, Meng S, Xu X, Xie J, Guo F, Yang Y, Qiu H, Liu L. 2019. Mesenchymal
908 stem cells induce dendritic cell immune tolerance via paracrine hepatocyte growth
909 factor to alleviate acute lung injury. *Stem Cell Res Ther*. doi:10.1186/s13287-019-1488-
910 2

911 Manson JJ, Crooks C, Naja M, Ledlie A, Goulden B, Liddle T, Khan E, Mehta P, Martin-
912 Gutierrez L, Waddington KE, Robinson GA, Ribeiro Santos L, McLoughlin E, Snell A,
913 Adeney C, Schim van der Loeff I, Baker KF, Duncan CJA, Hanrath AT, Lendrem BC,
914 De Soyza A, Peng J, J'Bari H, Greenwood M, Hawkins E, Peckham H, Marks M,
915 Rampling T, Luintel A, Williams B, Brown M, Singer M, West J, Jury EC, Collin M,
916 Tattersall RS. 2020. COVID-19-associated hyperinflammation and escalation of patient
917 care: a retrospective longitudinal cohort study. *Lancet Rheumatol*. doi:10.1016/S2665-
918 9913(20)30275-7

919 Mauracher L-M, Krall M, Roiß J, Hell L, Koder S, Hofbauer TM, Gebhart J, Hayden H,
920 Brostjan C, Ay C, Pabinger I. 2020. Neutrophil subpopulations and their activation
921 potential in patients with antiphospholipid syndrome and healthy individuals.
922 *Rheumatology*. doi:10.1093/rheumatology/keaa532

923 McInnes L, Healy J, Melville J. 2018. UMAP: Uniform manifold approximation and projection
924 for dimension reduction. *arXiv*.

925 Morrissey SM, Geller AE, Hu X, Tieri D, Cooke EA, Ding C, Woeste M, Zhange H, Cavallazi
926 R, Clifford SP, Chen J, Kong M, Watson CT, Huang J, Yan J. 2020. Emergence of Low-
927 density Inflammatory Neutrophils Correlates with Hypercoagulable State and Disease
928 Severity in COVID-19 Patients. *medRxiv* 2020.05.22.20106724.
929 doi:10.1101/2020.05.22.20106724

930 Ohnishi T, Kakimoto K, Bandow K, Lowenstein CJ, Daikuhara Y, Matsuguchi T. 2006.
931 Mature Hepatocyte Growth Factor/Scatter Factor on the Surface of Human

Granulocytes Is Released by a Mechanism Involving Activated Factor Xa. *J Immunol* **176**:6945–6953. doi:10.4049/jimmunol.176.11.6945

Parrot T, Gorin JB, Ponzetta A, Maleki KT, Kammann T, Emgård J, Perez-Potti A, Sekine T, Rivera-Ballesteros O, Gredmark-Russ S, Rooyackers O, Folkesson E, Eriksson LI, Norrby-Teglund A, Ljunggren HG, Björkström NK, Aleman S, Buggert M, Klingström J, Strålin K, Sandberg JK, Sandberg JT, Bergsten H, Björkström NK, Brighenti S, Buggert M, Butrym M, Chambers BJ, Chen P, Cornillet M, Cuapio A, Lozano ID, Dzidic M, Emgård J, Flodström-Tullberg M, Gorin JB, Gredmark-Russ S, Haroun-Izquierdo A, Hertwig L, Kalsum S, Klingström J, Kokkinou E, Kvedaraite E, Ljunggren HG, Lourda M, Maleki KT, Malmberg KJ, Michaëlsson J, Mjösberg J, Moll K, Muvva JR, Norrby-Teglund A, Palma Medina LM, Parrot T, Radler L, Ringqvist E, Sandberg JK, Sekine T, Soini T, Svensson M, Tynell J, Von Kries A, Wullimann D, Perez-Potti A, Rivera-Ballesteros O, Maucourant C, Varnaite R, Akber M, Berglin L, Brownlie D, Loreti MG, Sohlberg E, Kammann T, Henriksson E, Marquardt N, Strålin K, Aleman S, Sönnerborg A, Dillner L, Färnert A, Glans H, Nauclér P, Rooyackers O, Mårtensson J, Eriksson LI, Persson BP, Grip J, Unge C. 2020. MAIT cell activation and dynamics associated with COVID-19 disease severity. *Sci Immunol*. doi:10.1126/SCIIMMUNOL.ABE1670

Radermecker C, Detrembleur N, Guiot J, Cavalier E, Henket M, d'Emal C, Vanwinge C, Cataldo D, Oury C, Delvenne P, Marichal T. 2020. Neutrophil extracellular traps infiltrate the lung airway, interstitial, and vascular compartments in severe COVID-19. *J Exp Med*. doi:10.1084/jem.20201012

Ragab D, Salah Eldin H, Taeimah M, Khattab R, Salem R. 2020. The COVID-19 Cytokine Storm; What We Know So Far. *Front Immunol*. doi:10.3389/fimmu.2020.01446

Rosales C. 2018. Neutrophil: A cell with many roles in inflammation or several cell types? *Front Physiol*. doi:10.3389/fphys.2018.00113

Salamone G, Giordano M, Trevani AS, Gamberale R, Vermeulen M, Schettinni J, Geffner JR. 2001. Promotion of Neutrophil Apoptosis by TNF-α. *J Immunol*. doi:10.4049/jimmunol.166.5.3476

Silvin A, Chapuis N, Dunsmore G, Goubet AG, Dubuisson A, Derosa L, Almire C, Hénon C, Kosmider O, Droin N, Rameau P, Catelain C, Alfaro A, Dussiau C, Friedrich C, Sourdeau E, Marin N, Szwebel TA, Cantin D, Mouthon L, Borderie D, Deloger M, Bredel D, Mouraud S, Drubay D, Andrieu M, Lhonneur AS, Saada V, Stoclin A, Willekens C, Pommeret F, Griscelli F, Ng LG, Zhang Z, Bost P, Amit I, Barlesi F, Marabelle A, Pène F, Gachot B, André F, Zitvogel L, Ginhoux F, Fontenay M, Solary E. 2020. Elevated Calprotectin and Abnormal Myeloid Cell Subsets Discriminate Severe from Mild COVID-19. *Cell*. doi:10.1016/j.cell.2020.08.002

Small N, Lung C. 2006. Correspondence.

Song B, Lee JM, Park YJ, Kim IK, Kim BS, Shin KS, Jeon I, Koh CH, Bae EA, Seo H, Byun Y, Kang CY. 2020. Differentiation of c-Kit+CD24+ natural killer cells into myeloid cells in a GATA-2-dependent manner. *FASEB J*. doi:10.1096/fj.201902662R

Ui Mhaonaigh A, Coughlan AM, Dwivedi A, Hartnett J, Cabral J, Moran B, Brennan K, Doyle SL, Hughes K, Lucey R, Floudas A, Fearon U, McGrath S, Cormican S, De Bhailis A, Molloy EJ, Brady G, Little MA. 2019. Low Density Granulocytes in ANCA Vasculitis Are Heterogenous and Hypo-Responsive to Anti-Myeloperoxidase Antibodies. *Front Immunol*. doi:10.3389/fimmu.2019.02603

Van Den Hoogen LL, Van Der Linden M, Meyaard L, Fritsch-Stork RDE, Van Roon JA, Radstake TRDJ. 2020. Neutrophil extracellular traps and low-density granulocytes are associated with the interferon signature in systemic lupus erythematosus, but not in

antiphospholipid syndrome. *Ann Rheum Dis*. doi:10.1136/annrheumdis-2019-215781

Villani AC, Satija R, Reynolds G, Sarkizova S, Shekhar K, Fletcher J, Griesbeck M, Butler A, Zheng S, Lazo S, Jardine L, Dixon D, Stephenson E, Nilsson E, Grundberg I, McDonald D, Filby A, Li W, De Jager PL, Rozenblatt-Rosen O, Lane AA, Haniffa M, Regev A, Hacohen N. 2017. Single-cell RNA-seq reveals new types of human blood dendritic cells, monocytes, and progenitors. *Science (80-)*. doi:10.1126/science.aah4573

Voron T, Colussi O, Marcheteau E, Pernot S, Nizard M, Pointet AL, Latreche S, Bergaya S, Benhamouda N, Tanchot C, Stockmann C, Combe P, Berger A, Zinzindohoue F, Yagita H, Tartour E, Taieb J, Terme M. 2015. VEGF-A modulates expression of inhibitory checkpoints on CD8++ T cells in tumors. *J Exp Med*. doi:10.1084/jem.20140559

Wang J, Li Q, Yin Y, Zhang Y, Cao Y, Lin X, Huang L, Hoffmann D, Lu M, Qiu Y. 2020. Excessive Neutrophils and Neutrophil Extracellular Traps in COVID-19. *Front Immunol*. doi:10.3389/fimmu.2020.02063

Weerahandi H, Hochman KA, Simon Emma, Blaum C, Chodosh J, Duan E, Garry K, Kahan T, Karmen-Tuohy S, Karpel H, Mendoza F, Prete AM, Quintana L, Rutishauser J, Santos Martinez L, Shah K, Sharma S, Simon Elias, Stirniman A, Horwitz L. 2020. Post-discharge health status and symptoms in patients with severe COVID-19. *medRxiv Prepr Serv Heal Sci*. doi:10.1101/2020.08.11.20172742

Wilk AJ, Rustagi A, Zhao NQ, Roque J, Martínez-Colón GJ, McKechnie JL, Ivison GT, Ranganath T, Vergara R, Hollis T, Simpson LJ, Grant P, Subramanian A, Rogers AJ, Blish CA. 2020. A single-cell atlas of the peripheral immune response in patients with severe COVID-19. *Nat Med*. doi:10.1038/s41591-020-0944-y

Wislez M, Rabbe N, Marchal J, Milleron B, Crestani B, Mayaud C, Antoine M, Soler P, Cadranel J. 2003. Hepatocyte growth factor production by neutrophils infiltrating bronchioloalveolar subtype pulmonary adenocarcinoma: Role in tumor progression and death. *Cancer Res*.

Woodruff MC, Ramonell RP, Nguyen DC, Cashman KS, Saini AS, Haddad NS, Ley AM, Kyu S, Howell JC, Ozturk T, Lee S, Suryadevara N, Case JB, Bugrovsky R, Chen W, Estrada J, Morrison-Porter A, Derrico A, Anam FA, Sharma M, Wu HM, Le SN, Jenks SA, Tipton CM, Staitieh B, Daiss JL, Ghosn E, Diamond MS, Carnahan RH, Crowe JE, Hu WT, Lee FEH, Sanz I. 2020. Extrafollicular B cell responses correlate with neutralizing antibodies and morbidity in COVID-19. *Nat Immunol*. doi:10.1038/s41590-020-00814-z

Xu Z, Shi L, Wang Y, Zhang J, Huang L, Zhang C, Liu S, Zhao P, Liu H, Zhu L, Tai Y, Bai C, Gao T, Song J, Xia P, Dong J, Zhao J, Wang FS. 2020. Pathological findings of COVID-19 associated with acute respiratory distress syndrome. *Lancet Respir Med*. doi:10.1016/S2213-2600(20)30076-X

Yao XH, Li TY, He ZC, Ping YF, Liu HW, Yu SC, Mou HM, Wang LH, Zhang HR, Fu WJ, Luo T, Liu F, Chen C, Xiao HL, Guo HT, Lin S, Xiang DF, Shi Y, Li QR, Huang X, Cui Y, Li XZ, Tang W, Pan PF, Huang XQ, Ding YQ, Bian XW. 2020. [A pathological report of three COVID-19 cases by minimally invasive autopsies]. *Zhonghua bing li xue za zhi = Chinese J Pathol*. doi:10.3760/cma.j.cn112151-20200312-00193

Young Barnaby E., Ong SWX, Ng LF, Anderson DE, Chia WN, Chia PY, Ang LW, Mak T-M, Kalimuddin S, Chai LYA, Pada S, Tan SY, Sun L, Parthasarathy P, Fong S-W, Chan Y-H, Tan CW, Lee B, Rötzschke O, Ding Y, Tambyah P, Low JG, Cui L, Barkham T, Lin RTP, Leo Y-S, Renia L, Wang L-F, Lye DC. 2020. Immunological and Viral Correlates of COVID-19 Disease Severity: A Prospective Cohort Study of the First 100 Patients in Singapore. *SSRN Electron J*. doi:10.2139/ssrn.3576846

Young Barnaby E, Ong SWX, Ng LFP, Anderson DE, Chia WN, Chia PY, Ang LW, Mak T-M, Kalimuddin S, Chai LYA, Pada S, Tan SY, Sun L, Parthasarathy P, Fong S-W, Chan Y-H, Tan CW, Lee B, Rötzschke O, Ding Y, Tambyah P, Low JGH, Cui L, Barkham T, Lin RTP, Leo Y-S, Renia L, Wang L-F, Lye DC, Lim PL, Peng Ang BS, Lee CC, U Lee LS, Ling LM, Ng OT, Chan M, Marimuthu K, Vasoo S, Wong CS, Lee TH, Sadarangani S, Lin RJ, Sadasiv MS, Ling Ng DH, Choy CY, En Tan GS, Tan YK, Sutjipto S, Lee PH, Tay JY, Yeo TW, Khoo BY, Tay WC, Ng G, Mah YY, Tan W, De PP, Pooja R, Chia JWZ, Constance Chen YY, Mendis S, Toh BK, Choon Fong RK, Lin Oh HM, Fong Chien JM, Shafi H, Cheong HY, Tan TY, Tan TT, Tan BH, Wijaya L, Venkatachalam I, Chua YY, Zhi Cherng BP, Zi Chan YF, Wong HM, Thien SY, Meng Goh KC, Ling Tan SY, Ean Oon LL, Chan KS, Lin L, Gin Chan DS, Ooi ST, Narayana DR, Somani J, Ling Oon JE, Yan GZ, Allen DM, Jureen R, Yan B, Foo R, Kang A, Sivalingam V, How W, Fernandez NL, Yeo NK-W, Chee RS-L, Amrun SN, Lim PL, Peng Ang BS, Lee CC, U Lee LS, Ling LM, Ng OT, Chan M, Marimuthu K, Vasoo S, Wong CS, Lee TH, Sadarangani S, Lin RJ, Sadasiv MS, Ling Ng DH, Choy CY, En Tan GS, Tan YK, Sutjipto S, Lee PH, Tay JY, Yeo TW, Khoo BY, Tay WC, Ng G, Mah YY, Tan W, De PP, Pooja R, Chia JWZ, Constance Chen YY, Mendis S, Toh BK, Choon Fong RK, Lin Oh HM, Fong Chien JM, Shafi H, Cheong HY, Tan TY, Tan TT, Tan BH, Wijaya L, Venkatachalam I, Chua YY, Zhi Cherng BP, Zi Chan YF, Wong HM, Thien SY, Meng Goh KC, Ling Tan SY, Ean Oon LL, Chan KS, Lin L, Gin Chan DS, Ooi ST, Narayana DR, Somani J, Ling Oon JE, Yan GZ, Allen DM, Jureen R, Yan B, Foo R, Kang A, Sivalingam V, How W, Fernandez NL, Yeo NK-W, Chee RS-L, Amrun SN. 2020. Viral Dynamics and Immune Correlates of Coronavirus Disease 2019 (COVID-19) Severity. *Clin Infect Dis*. doi:10.1093/cid/ciaa1280

Yu Y, Su K. 2013. Neutrophil Extracellular Traps and Systemic Lupus Erythematosus. *J Clin Cell Immunol*. doi:10.4172/2155-9899.1000139

Zhou Y, Fu B, Zheng X, Wang D, Zhao C, Qi Y, Sun R, Tian Z, Xu X, Wei H. 2020. Pathogenic T-cells and inflammatory monocytes incite inflammatory storms in severe COVID-19 patients. *Natl Sci Rev*. doi:10.1093/nsr/nwaa041

Supplemental Information

Data-driven analysis of COVID-19 reveals specific severity patterns distinct from the temporal immune response

Jackwee Lim, Kia Joo Puan, Liang Wei Wang, Karen Wei Weng Teng, Chiew Yee Loh, Kim Peng Tan, Guillaume Carissimo, Yi-Hao Chan, Chek Meng Poh, Cheryl Yi-Pin Lee, Siew-Wai Fong, Nicholas Kim-Wah Yeo, Rhonda Sin-Ling Chee, Siti Naqiah Amrun, Zi Wei Chang, Matthew Zirui Tay, Anthony Torres-Ruesta, Norman Leo Fernandez, Wilson How, Anand K. Andiappan, Wendy Lee, Kaibo Duan, Seow-Yen Tan, Gabriel Yan, Shirin Kalimuddin, David Chien Lye, Yee-Sin Leo, Sean W. X. Ong, Barnaby E. Young, Laurent Renia, Lisa F.P. Ng, Bernett Lee, Olaf Rötzschke

Figure S1. Temporal changes in surface marker expression profiles of various immune cell subsets during active and convalescent COVID-19.

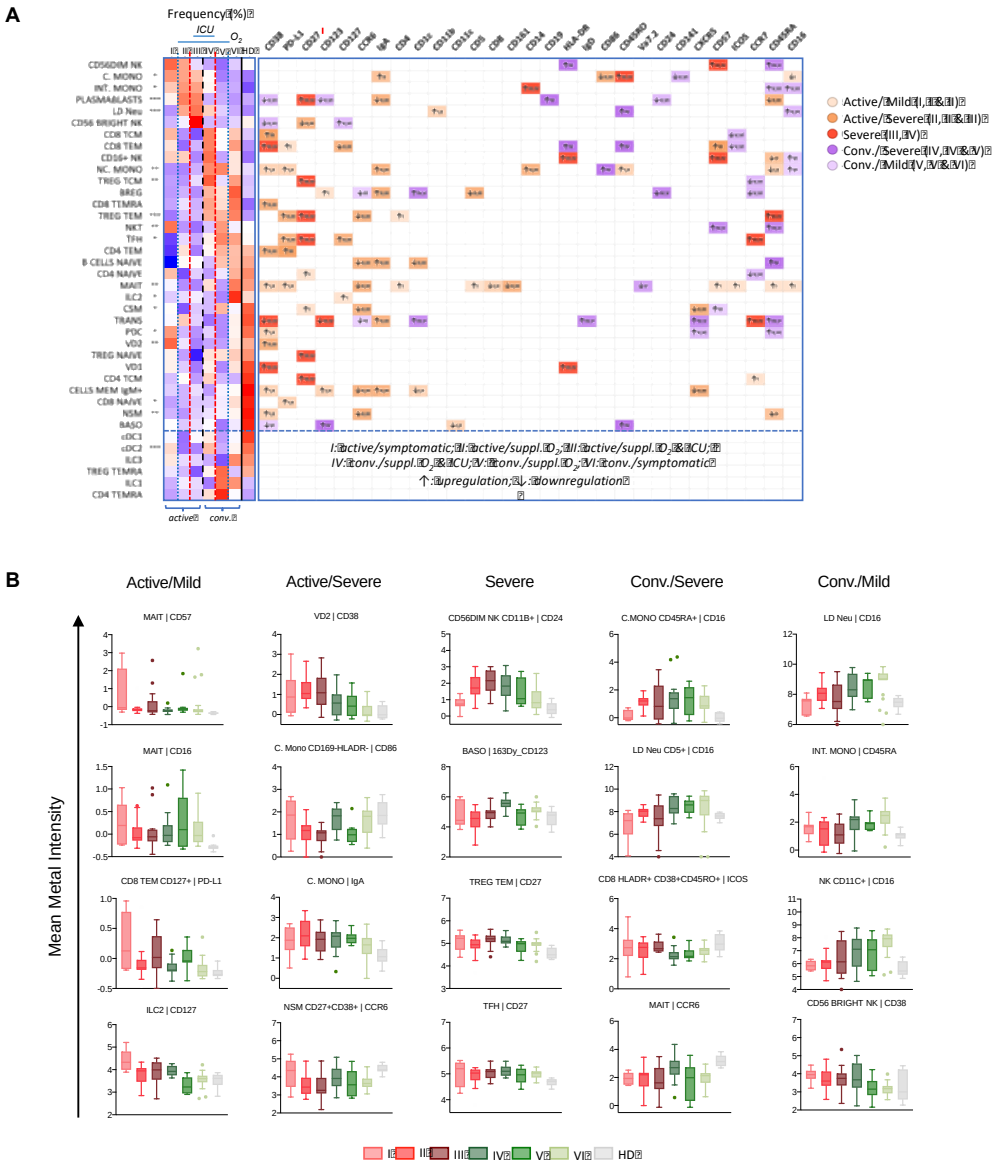

Figure S2. Alterations of immune cell types dynamics and immunotypes associated with mild and severe during active and convalescent infection. (A) Left: Heat map representation of frequencies of 38 main immune cell populations among the 6 groups severity stratifications. Right: up- or down-regulation of indicated surface markers for the 38 main immune cell populations among 6 group severity stratifications. Asterisks indicate statistical significance - *, p<0.05; **, p<0.01; ***, p<0.001 (one-way ANOVA of all disease phases and healthy controls). (B) Box-and-whiskers plots of selected immunotypes showing means and IQR up-regulation and down-regulation of surface markers associated with active/mild, active/severe, severe, conv./severe, and conv./mild clinical states.

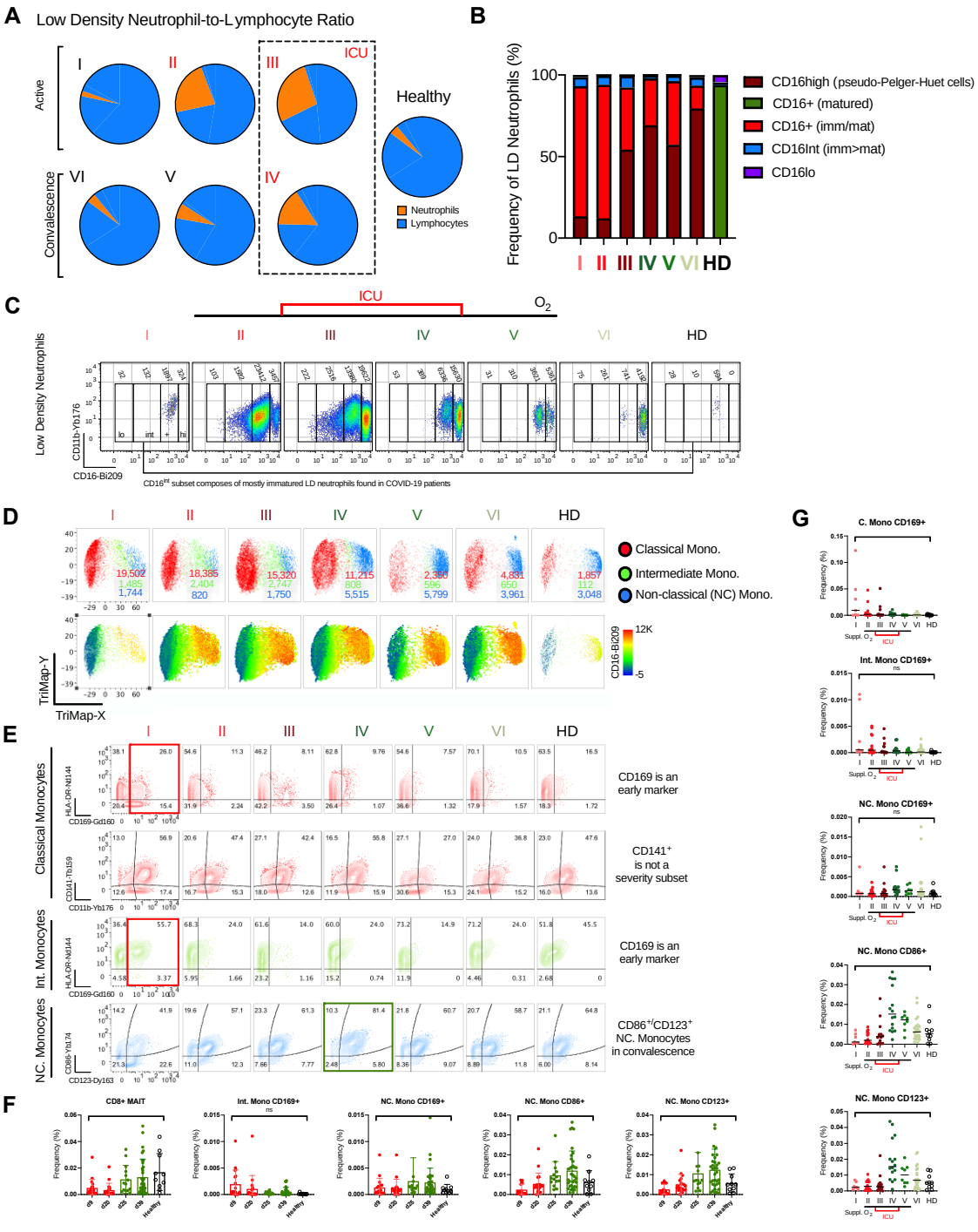

Figure S3. Neutrocytosis and monocytosis during SARS-CoV-2 infection. (A) Neutrocytosis due to SARS-CoV-2 infection is mild among symptomatic group I patients but persisted in severe convalescence group. A higher Low-Density Neutrophil-to-Lymphocyte Ratio is associated with disease severity. (B) Frequency distribution of Low-Density Neutrophil subsets whereby the $CD16^{+}$ LD neutrophils are mostly mature neutrophils in healthy donors but co-mixed with immature neutrophils from the $CD16^{int}$ LD neutrophil subset in COVID-19

patients. The presence of $CD16^{++/high}$ LD neutrophils described as pseudo-Pelger-Huet cells, are absent in healthy donors. (C) The pseudo-coloured plots of LD neutrophil gated as $CD16^{lo}$, left shift $CD16^{int}$, $CD16^{+}$ and $CD16^{high}$ subsets and their indicated cell count out of 210K human PBMCs. (D) Monocytosis is apparent even in symptomatic group I and decreases with convalescence with CD16 marker upregulation in NC. Monocytes. (E) Comparison of NC. monocytes and other monocytes associated with convalescence and COVID-19 disease severity. Scatter plots depict the means with SEM. ns: not significant, *, p <0.03; **, p <0.002; ***, p <0.0002, ****, p <0.0001 (Kruskal-Wallis test with multiple comparisons performed on each disease severity group versus total healthy). (F-G) Frequency changes of representing monocyte subsets associated with surface markers during (F) SARS-CoV-2 infection and (G) COVID-19 severity.

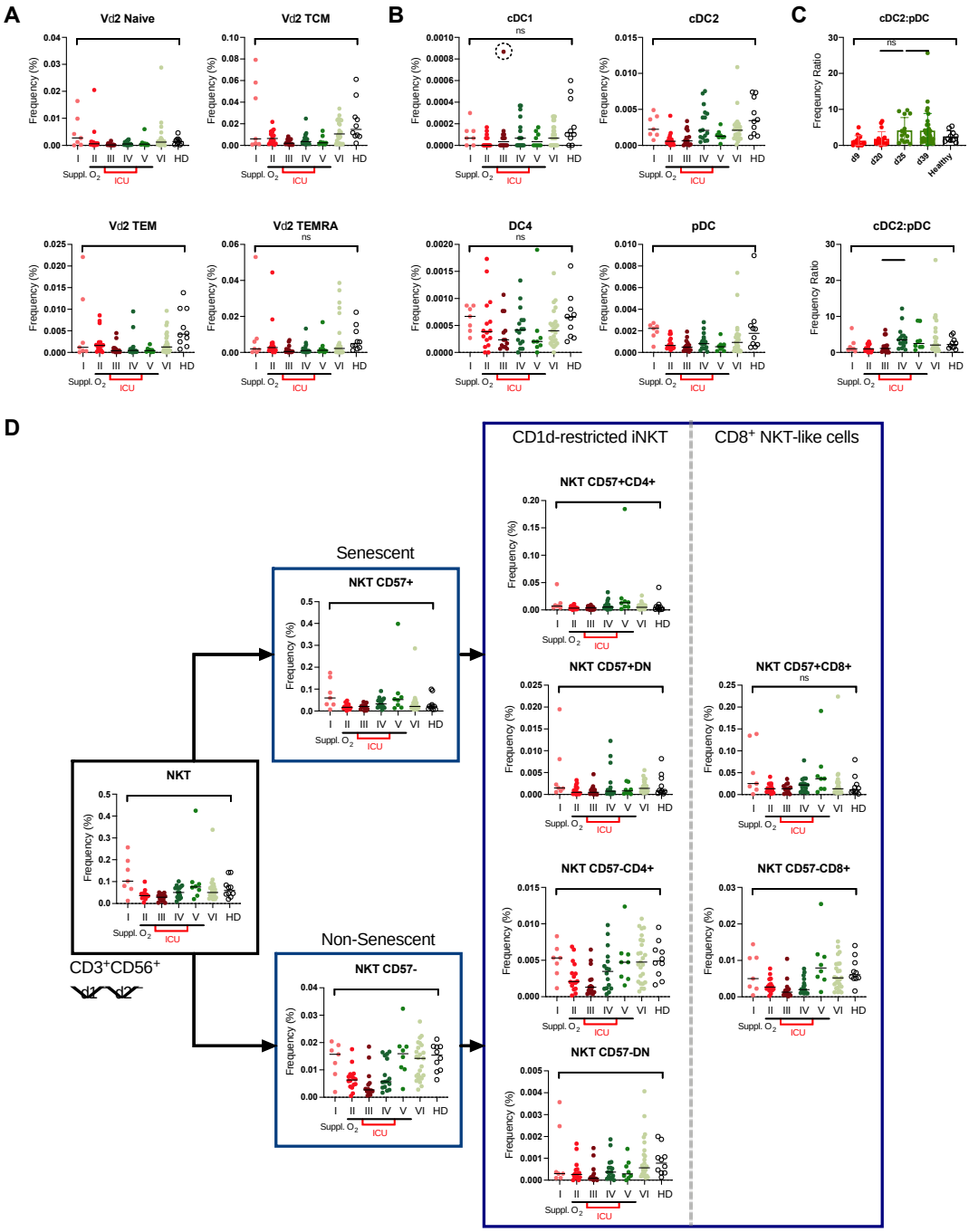

Figure S4. COVID-19 severity is specific to selected Vδ2 T, dendritic cell and non-senescent NKT cell subsets. Overview of frequency changes across the (A) Vδ2 T cells and (B) dendritic cells showing insignificance of subsets selected based on p-values. Scatter plots depict the means with SEM. ns: not significant,*, p <0.03; **, p <0.002; ***, p <0.0002, ****, p <0.0001 (Kruskal-Wallis test with multiple comparisons performed on each disease severity group versus total healthy). An extreme outlier due to a single patient in cDC1 is encircled.

Vδ1 T cell subsets are insignificant and thus not shown. (C) The ratio of cDC2: pDC frequency during COVID-19 infection. (D) Clustering of NKT gated based on $CD3^+CD56^+V\delta1^-V\delta2^-$ T cell subsets into invariant NKT (iNKT) and CD1d-unrestricted CD8+ NKT-like cells gated based on senescent marker CD57. The three human NKT subsets ($CD4^+$, $CD8^+$ and $CD4^-CD8^-$/DN) also consist of Type I presenting invariant Vα24Jα18 TCR and Type II presenting a diverse TCR repertoire, which are undefined in this work.

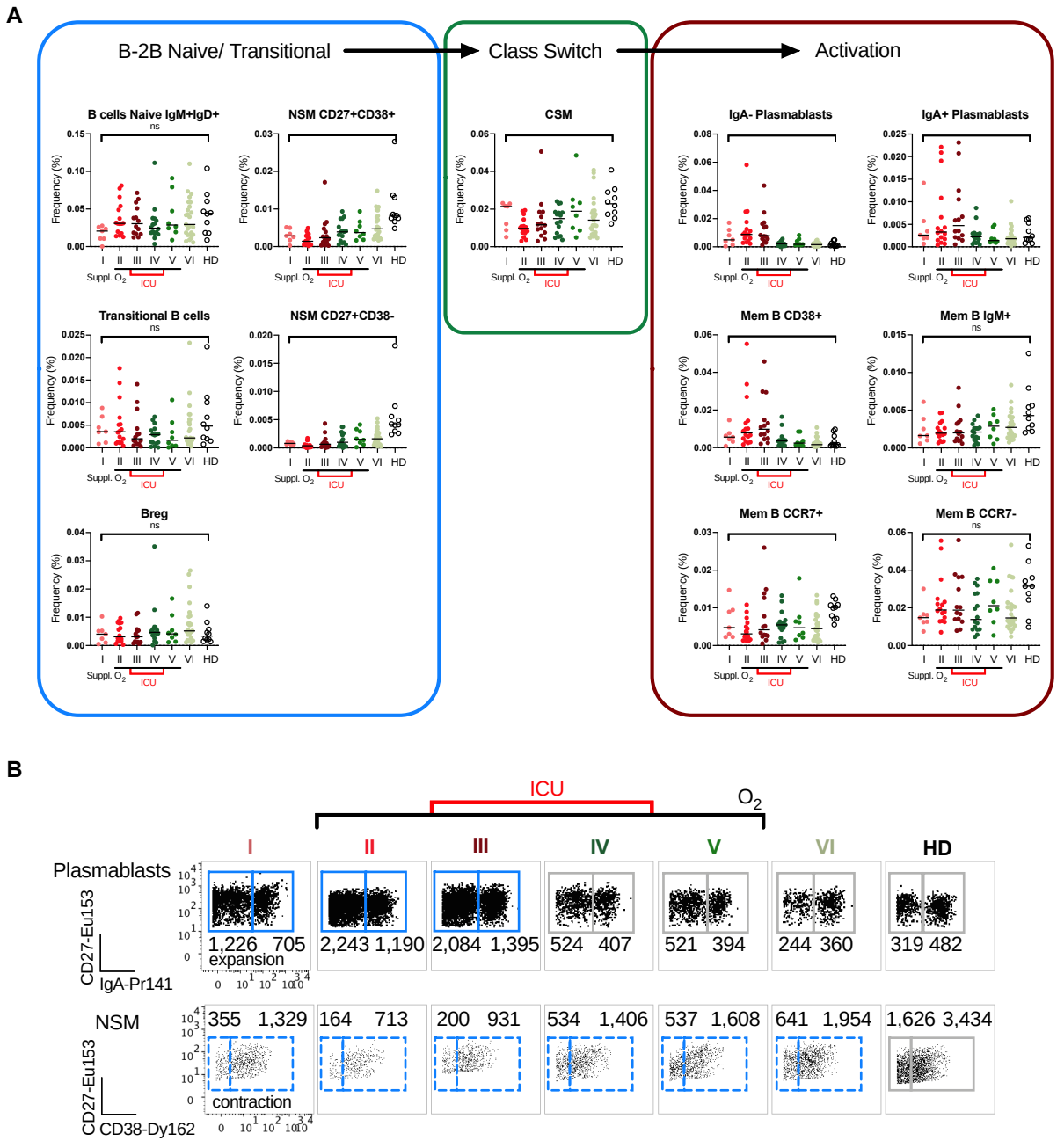

Figure S5. Heterogeneous B cell subset development during SARS-CoV-2 infection. (A) Scatterplots of B cell subset frequencies from Naïve to Memory based on COVID-19 severity. Scatterplots depict the means with SEM. ns: not significant, *, p <0.03; **, p <0.002; ***, p <0.0002, ****, p <0.0001 (Kruskal-Wallis test with multiple comparisons performed on each disease severity group versus total healthy). (B) Dotplots of representative B cell subsets for either expanded or contracted cell population in response to SARS-CoV-2 infection. The absolute numbers of cells out of 300,000 PBMCs are shown.

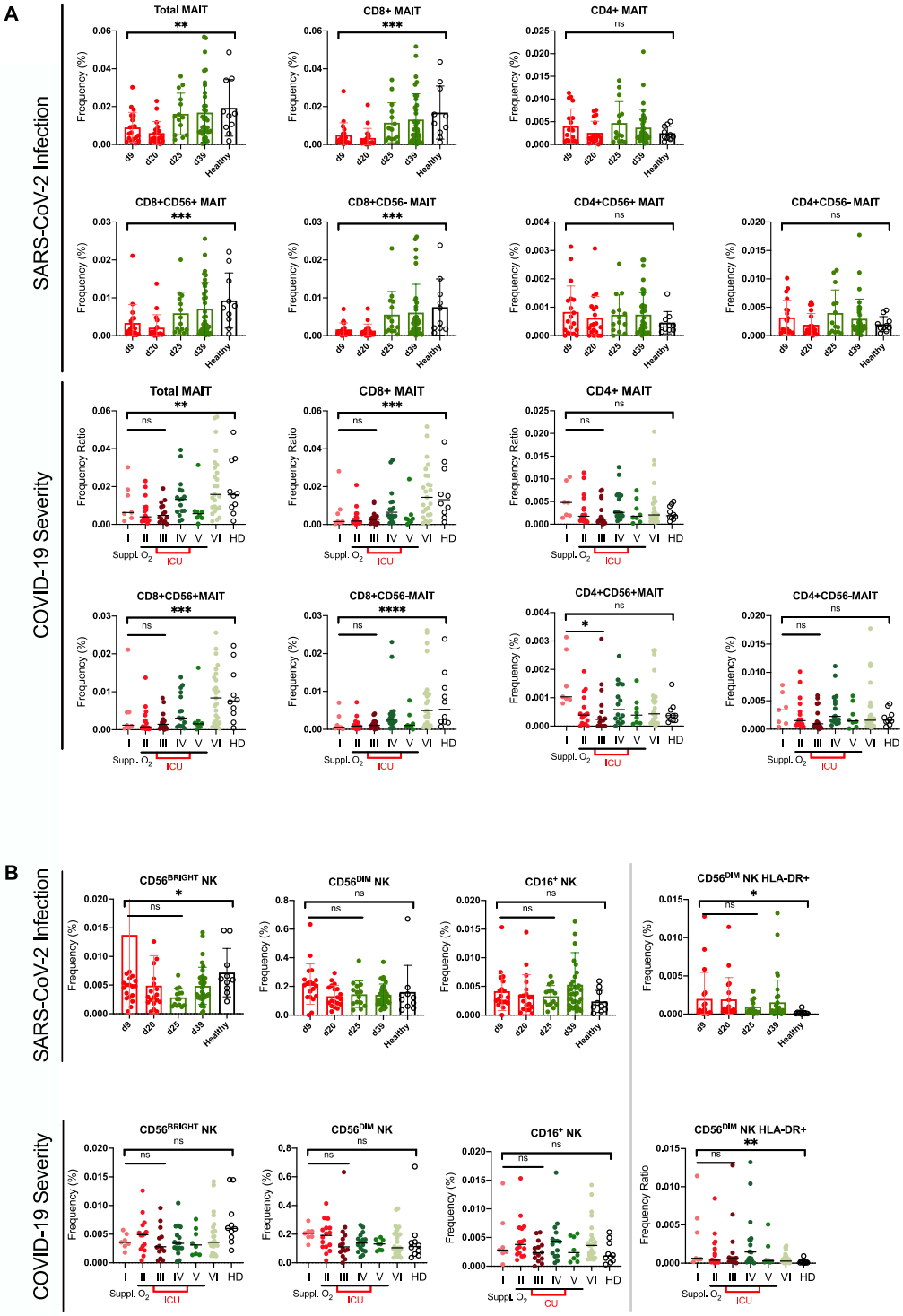

Figure S6. Loss of CD8^{+} MAIT and CD56^{Bright} NK cells are innate-like responses to SARS-CoV-2 infection but not severity. (A) Frequencies of MAIT cell subsets based on disease stage from early active to late convalescence. CD8^{+} but not CD4^{+} MAIT cells are significantly reduced during SARS-CoV-2 infection, which recover with health. Also, frequencies of different MAIT cell subsets with disease severity. There is little or no significance among

1189 severity groups I, II and III. (B) The depletion of $CD56^{Bright}$ NK subpopulation when compared
1190 to healthy does not associate with COVID-19 disease severity. Also, $CD56^{Dim}$ NK $HLA\text{-}DR^{+}$
1191 subset is not strongly correlated to disease severity. Scatter plots depict the means with
1192 SEM. ns: not significant, *, p <0.03; **, p <0.002; ***, p <0.0002, ****, p <0.0001 (Kruskal-
1193 Wallis test with multiple comparisons performed on each disease severity group versus total
1194 healthy).

1195

1196

1197

1198

1199

1200

1201

1202

1203

1204

1205

1206

1207

1208

1209

1210

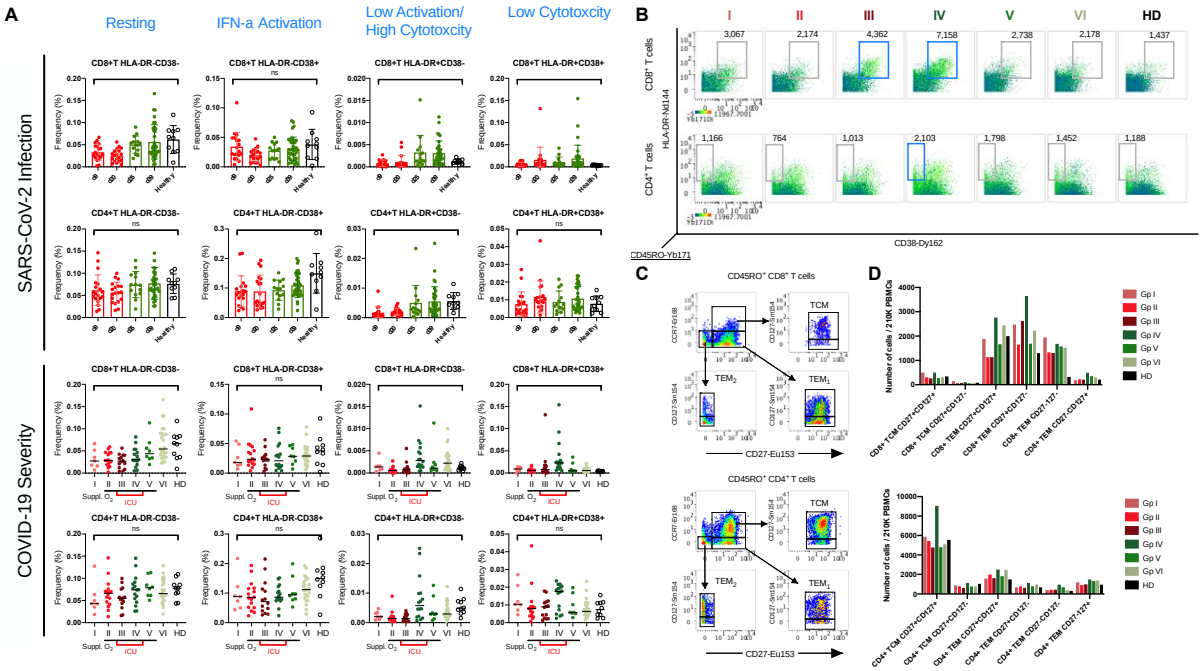

Figure S7. Heterogeneous T cell activation during SARS-CoV-2 infection. (A) Frequencies of $CD4^+$ and $CD8^+$ T cells based on HLA-DR and CD38 cell surface markers. Lymphopenia is apparent during active SARS-CoV-2 infection and T lymphocyte number increases in convalescence. Disease severity grouping further delineates finer structures. The $CD8^+$ T cell subpopulations e.g. $HLA\text{-}DR^+CD38^+$ $CD8^+$ T subsets are elevated in COVID-19 severity group IV. Scatter plots depict the means with SEM. ns: not significant, *, p <0.03; **, p <0.002; ***, p <0.0002, ****, p <0.0001 (Kruskal-Wallis test with multiple comparisons performed on each disease severity group versus total healthy). (B) 3-dimensional dotplots of statistically significant $HLA\text{-}DR^+CD38^+$ $CD8^+$ and $HLA\text{-}DR^+CD38^-$ $CD4^+$ T subset against memory $CD45RO^+$ antigen. (C) Gating strategies for memory T subsets. (D) Barplot of total memory $CD8^+/CD4^+$ T subsets (TCM and TEM) and the CD27 and CD127 surface markers across disease severity groups showing similarities and differences among COVID-19 patients and healthy donors.

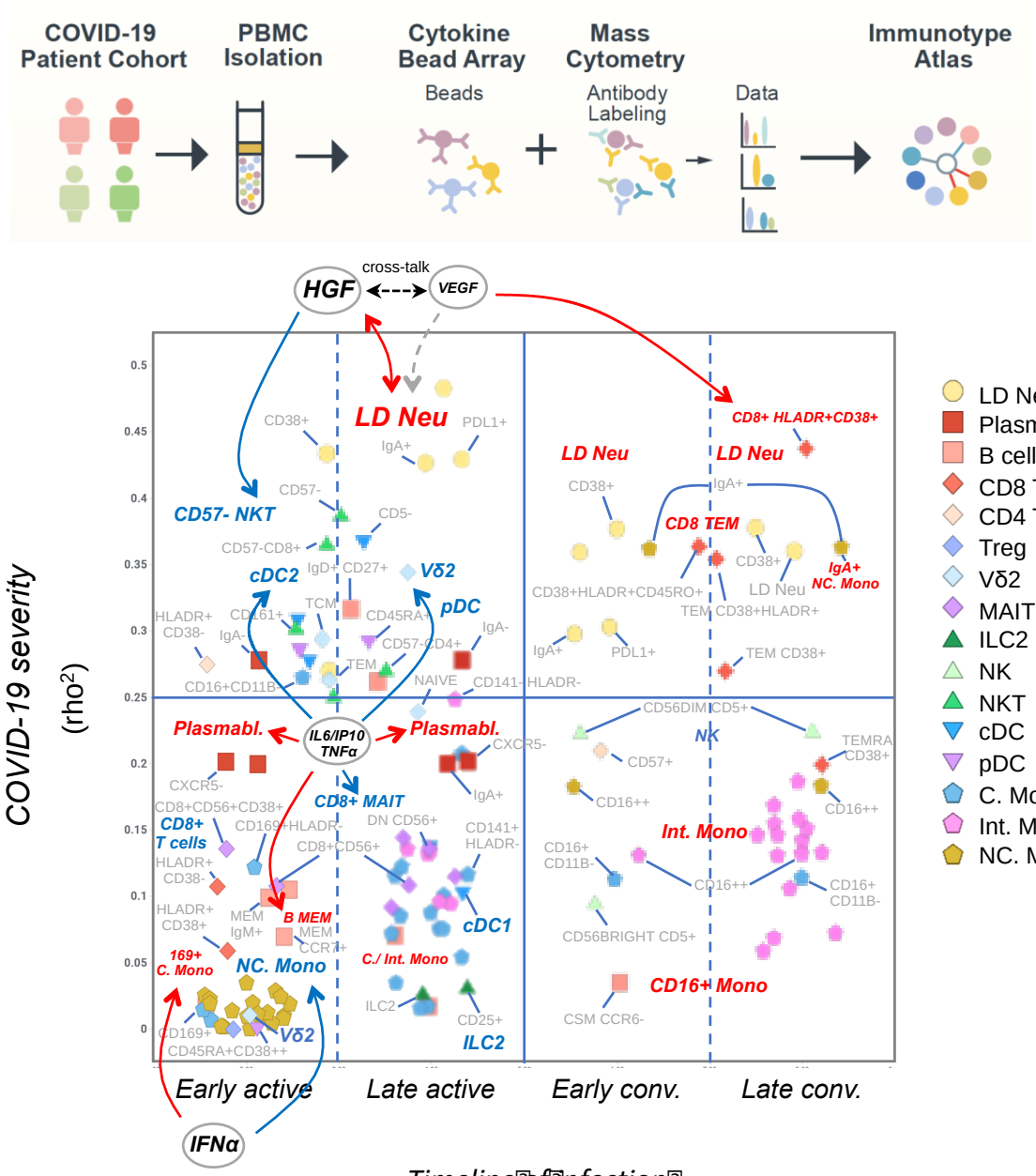

Figure S8. Timeline of infection and impact on COVID-19 disease severity. The figure is a summary of the timeline of infection versus the severity of COVID-19. The timeline is broken down into four phases (early active, late active, early conv. and late conv.), which were used to bin the extended set of 327 immune cells. The disease severity is expressed as the rho^2 value from the correlation of their cell frequencies with the severity score. Shown are only cell subsets which have at least a 3-fold change in frequency in the respective phase (compare figures 7A and 7B) and/or a rho^2 value > 0.25 for the disease correlation (compare figures 7C and 7D). The name of key cell subsets with increased blood frequencies are

1237 labeled in red, subsets with decreased frequency in blue. Cell subset/cytokine interactions

1238 are taken from figure 7.

Variables	Healthy Control (N = 10)	COVID-19					
		Total (N = 77)	Statistical testing of total COVID-19 vs healthy controls (two-tailed p-value)	MILD (No O_2 Supplementation) - Groups I and VI (N = 31)	MODERATE (O_2 Supplementation) - Groups II and V (N = 20)	SEVERE (O_2 Supplementation + ICU) - Groups III and IV (N = 26)	Statistical testing of severity groups (two-tailed p-value, if applicable)
Sex - No. (%)							
Male	6 (60.0)	60 (77.9)	0.2128 (χ2 test)	20 (64.5)	17 (85.0)	23 (88.5)	0.0814 (χ2 test)
Female	4 (40.0)	17 (22.1)		11 (35.5)	3 (15.0)	3 (11.5)	
Age - Years							
Mean ± SD.	36.6 ± 9.2	50.4 ± 14.7	0.007 (MW U test)	43.0 ± 13.0	52.9 ± 13.6	57.4 ± 13.9	<0.0001 (KW test with Dunn's multiple comparison)
Median (IQR)	34.0 (30.75-41.25)	51.0 (39.5-62.0)		44.0 (30.0-54.0)	53.0 (42.5-62.5)	60.5 (45.0-66.5)	
Range	25.0-56.0	24.0-82.0		24.0-65.0	28.0-80.0	29.0-82.0	
Time from Onset to Admission, Days							
Mean ± SD.				5.0 ± 8.1	5.4 ± 6.6	4.8 ± 3.4	0.528 (KW test with Dunn's multiple comparison)
Median (IQR)				3.0 (1.0-5.0)	4.0 (2.0-7.0)	3.0 (2.0-9.0)	
Range				0.0-45.0	1.0-31.0	0.0-10.0	

Time from Admission to ICU, Days							
Mean ± SD.						2.4 ± 1.8	
Median (IQR)						2.0 (1.0-4.0)	
Range						0.0-6.0	
Duration under Intubation, Days							
Mean ± SD.						7.9 ± 18.8	
Median (IQR)						1.5 (0.0-7.75)	
Range						0.0-95.0*	
Significant Medical History - No. (%)							
Myocardial infarction		12 (15.6)		2 (6.5)	5 (25.0)	5 (19.2)	0.1673 (χ2 test)
Comorbidity - No. (%)†							
Hypertension		27 (35.1)		5 (16.1)	9 (45.0)	13 (50.0)	0.8734 (χ2 test)
Hyperlipidemia/ dyslipidemia		26 (33.8)		3 (9.7)	11 (55.0)	12 (46.2)	0.4603 (χ2 test)
Diabetes mellitus		18 (23.4)		1 (3.2)	6 (30.0)	11 (42.3)	0.5487 (χ2 test)

Table S1. Demographic details of the study subjects. Population variables (sex and age at admission) and clinical variables (time from symptom onset to hospital admission, time from hospital admission to ICU entry, period of intubation, significant medical history and existing comorbidities) are shown. IQR, interquartile range; KW test, Kruskal-Wallis test; MW U test, Mann-Whitney U test; SD, standard deviation. * Includes the sole outlier who was intubated for 95 days before passing away from COVID-19. † Each instance of comorbidity was counted, even in cases where a patient had multiple comorbidities.

	B cells	**Abbrev.**	**CD45$^+$CD3$^-$**
1	Naïve	-	CD19$^+$CD27$^-$IgM$^+$IgD$^+$
2	Transitional	Trans.	CD19$^+$CD27$^-$IgM$^{+/bright}$CD38$^+$CD24$^+$
3	Non-class-switched memory	NSM	CD19$^+$CD27$^+$IgM$^+$IgD$^+$CD38$^{+/-}$
4	Class switched memory	CSM	CD19$^+$CD27$^+$IgM$^-$IgD$^-$CD38$^{+/dim}$
5	IgM memory	IgM Mem	CD19$^+$CD27$^+$IgM$^+$IgD$^-$
6	Plasmablasts	-	CD19$^+$CD27$^{+/bright}$ IgM$^-$IgD$^-$CD38$^{+/bright}$ or TriMAP cluster
7	B regulatory	Breg	CD19$^+$CD27$^-$IgM$^{+/bright}$CD24$^{+/bright}$CD5$^+$
	T cells	**Abbrev.**	**CD45$^+$CD3$^+$**
8,9	Naïve	-	CD4$^+$ or CD8$^+$CD45RA$^+$CD45RO$^-$CCR7$^+$CD27$^+$
10,11	Central memory	CM	CD4$^+$ or CD8$^+$CD45RA$^-$CD45RO$^+$CCR7$^+$
12,13	Effector memory	EM	CD4$^+$ or CD8$^+$CD45RA$^-$CD45RO$^+$CCR7$^-$
14,15	Terminally differentiated effector memory	TEMRA	CD4$^+$ or CD8$^+$CD45RA$^+$CD45RO$^-$CCR7$^-$CD27$^-$
-	T regulatory	Treg	CD4$^+$CD25$^+$CD127$^{-/dim}$
16	Treg naive	-	Treg| CD45RA$^+$CD45RO$^-$CCR7$^+$CD27$^+$
17	Treg CM	Treg CM	Treg| CD45RA$^-$CD45RO$^+$CCR7$^+$
18	Treg EM	Treg EM	Treg| CD45RA$^-$CD45RO$^+$CCR7$^-$
19	Treg Terminally differentiated effector memory	Treg TEMRA	Treg| CD45RA$^+$CD45RO$^-$CCR7$^-$CD27$^-$
20	Vδ1 T	-	CD4$^-$CD8$^-$TCRγδ$^+$Vδ1$^+$
21	Vδ2 T	-	CD4$^-$CD8$^-$TCRγδ$^+$Vδ2$^+$ or TriMAP cluster
22	Germinal center resident T follicular helper	T_{FH}	CD4$^+$CD25$^-$CXCR5$^+$CCR7$^-$CD127$^+$
23	Mucosal associated invariant T cells	MAIT	CD14$^-$CD19$^-$Vα7.2$^+$CD161$^{+/bright}$CD56$^{+/-}$
24	NKT	NKT	CD14$^-$CD19$^-$Vα7.2$^-$CD56$^+$
	TriMAP gating	**Abbrev.**	**From TriMAP clustering**
25	CD56^{Dim} NK	-	TriMAP| CD19$^-$CD14$^-$CD56$^+$CD16$^+$
26	CD56^{Bright} NK	-	TriMAP| CD19$^-$CD14$^-$CD56$^+$CD16$^-$
27	CD16$^+$ NK	-	TriMAP| CD19$^-$CD14$^-$CD56$^-$CD16$^+$
28	Classical Monocytes	C. Mono.	TriMAP| CD19$^-$CD14$^{+/bright}$CD16$^-$
29	Intermediate Monocytes	Int. Mono.	TriMAP| CD19$^-$CD14$^{+/bright}$CD16$^+$
30	Non-classical Monocytes	NC. Mono.	TriMAP| CD19$^-$CD14$^{+/dim}$CD16$^{+/bright}$
31	Plasmacytoid dendritic cells	pDC	TriMAP| HLA-DR$^+$CD11c$^-$CD123$^{+/bright}$CD45RA$^+$
32	Conventional type 1 dendritic cells	cDC1	TriMAP| HLA-DR$^+$CD11c$^+$CD1c$^-$CD141$^+$
33	Conventional type 2 dendritic cells	cDC2	TriMAP| HLA-DR$^+$CD11c$^+$CD141$^-$CD1c$^+$
34	Low-density neutrophils	LD. Neu	TriMAP| CD11b$^+$CD24$^+$ or CD66b$^+$CD15$^+$CD16^{high}CD10$^+$CD24$^+$
	Lineage-negative	**Lin-**	**CD3$^-$CD56$^-$CD19$^-$HLA-DR$^-$CD14$^-$CD123$^-$CD16$^-$**
35	Basophils	Baso.	Lin$^-$CD38$^+$CD123$^+$
36	Innate lymphoid cell type 1	ILC1	Lin$^-$CD5$^+$CD11c$^-$(CD4$^+$, CD8$^+$, CD4$^-$CD8$^-$)
37	Innate lymphoid cell type 2	ILC2	Lin$^-$CD5$^-$CD11c$^-$CD161$^{+/bright}$
38	Innate lymphoid cell type 3	ILC3	Lin$^-$CD5$^-$CD11c$^+$
	Exclusion		
-	Monocytic dendritic cell 4	DC4	TriMAP| HLA-DR$^+$CD11c$^+$CD141$^-$CD1c$^-$

Table S2. Gating strategy used for 38 basic immune subsets. For TriMAP gated subpopulations, the distinct clusters are calculated using TripMAP algorithm and confirmed based on their surface markers. (-) DC4 subset is excluded in analysis due to extreme low frequency.

Index	Alphabetical Order	Short name	Rank_num	Rank_name
1	CyTOF B CELLS	B CELLS	45	(45) B cells
2	CyTOF B CELLS CCR7-	B CELLS CCR7-	27	(27) B CCR7-
3	CyTOF B CELLS CCR7+	B CELLS CCR7+	18	(18) B CCR7+
4	CyTOF B CELLS CD38+	B CELLS CD38+	3	(3) B CD38+
5	CyTOF B CELLS CXCR5-	B CELLS CXCR5-	8	(8) B CXCR5-
6	CyTOF B CELLS CXCR5+	B CELLS CXCR5+	47	(47) B CXCR5+
7	CyTOF B CELLS IgA+CD38++	B CELLS IgA+CD38high	7	(7) B IgA+CD38++
8	CyTOF B CELLS IgD-CD27-	B CELLS IgD-CD27-	16	(16) B IgD-CD27-
9	CyTOF B CELLS IgD+	B CELLS IgD+	46	(46) B IgD+
10	CyTOF B CELLS IgD+CD27+	B CELLS IgD+CD27+	12	(12) B IgD+CD27+
11	CyTOF B CELLS IgD+CD38+	B CELLS IgD+CD38+	40	(40) B IgD+CD38+
12	CyTOF B CELLS IgM+	B CELLS IgM+	41	(41) B IgM+
13	CyTOF B CELLS IgM+CD123+	B CELLS IgM+CD123+	28	(28) B IgM+CD123+
14	CyTOF B CELLS IgM+CD38++	B CELLS IgM+CD38high	10	(10) B IgM+CD38++
15	CyTOF B CELLS IgA+	B CELLS IgA+	32	(32) B IgA+
16	CyTOF B CELLS MEM CCR7-	B CELLS MEM CCR7-	24	(24) B MEM CCR7-
17	CyTOF B CELLS MEM CCR7+	B CELLS MEM CCR7+	19	(19) B MEM CCR7+
18	CyTOF B CELLS MEM CD38++	B CELLS MEM CD38high	2	(2) B MEM CD38++
19	CyTOF B CELLS MEM CXCR5-	B CELLS MEM CXCR5-	5	(5) B MEM CXCR5-
20	CyTOF B CELLS MEM CXCR5+	B CELLS MEM CXCR5+	35	(35) B MEM CXCR5+
21	CyTOF B CELLS MEM IgM+	B CELLS MEM IgM+	36	(36) B MEM IgM+
22	CyTOF B CELLS MEM IgM+CXCR5-	B CELLS MEM IgM+CXCR5-	1	(1) B MEM IgM+CXCR5-
23	CyTOF B CELLS MEM IgM+CXCR5+	B CELLS MEM IgM+CXCR5+	25	(25) B MEM IgM+CXCR5+
24	CyTOF B CELLS NAIVE	B CELLS NAIVE	42	(42) B NAIVE
25	CyTOF B CELLS NAIVE CCR7-	B CELLS NAIVE CCR7-	37	(37) B NAIVE CCR7-
26	CyTOF B CELLS NAIVE CCR7+	B CELLS NAIVE CCR7+	15	(15) B NAIVE CCR7+
27	CyTOF B CELLS NAIVE CD123+	B CELLS NAIVE CD123+	30	(30) B NAIVE CD123+
28	CyTOF B CELLS NAIVE CD5-	B CELLS NAIVE CD5-	17	(17) B NAIVE CD5-
29	CyTOF B CELLS NAIVE CD5+	B CELLS NAIVE CD5+	22	(22) B NAIVE CD5+
30	CyTOF B CELLS NAIVE CXCR5-	B CELLS NAIVE CXCR5-	20	(20) B NAIVE CXCR5-
31	CyTOF B CELLS NAIVE IgM-	B CELLS NAIVE IgM-	33	(33) B NAIVE IgM-
32	CyTOF B CELLS NAIVE IgM+	B CELLS NAIVE IgM+	26	(26) B NAIVE IgM+
33	CyTOF B MEM	B CELLS MEM	34	(34) B MEM
34	CyTOF BASO	BASO	1	(1) BASO
35	CyTOF BREG	BREG	3	(3) BREG
36	CyTOF BREG CD123+	BREG CD123+	1	(1) BREG CD123+
37	CyTOF BREG CD38+	BREG CD38+	2	(2) BREG CD38+
38	CyTOF BREG PDL1	BREG PDL1	4	(4) BREG PDL1
39	CyTOF C. MONO	C. MONO	17	(17) C. Mono
40	CyTOF C. Mono CD141-	C. Mono CD141-	20	(20) C. Mono CD141-

41	CyTOF C. Mono CD141-CD11B-	C. Mono CD141-CD11B-	15	(15) C. Mono CD141-CD11B-
42	CyTOF C. Mono CD141-CD11B+	C. Mono CD141-CD11B+	18	(18) C. Mono CD141-CD11B+
43	CyTOF C. Mono CD141-HLADR-	C. Mono CD141-HLADR-	7	(7) C. Mono CD141-HLADR-
44	CyTOF C. Mono CD141-HLADR+	C. Mono CD141-HLADR+	31	(31) C. Mono CD141-HLADR+
45	CyTOF C. Mono CD141+	C. Mono CD141+	16	(16) C. Mono CD141+
46	CyTOF C. Mono CD141+CD11B-	C. Mono CD141+CD11B-	13	(13) C. Mono CD141+CD11B-
47	CyTOF C. Mono CD141+CD11B+	C. Mono CD141+CD11B+	19	(19) C. Mono CD141+CD11B+
48	CyTOF C. Mono CD141+HLADR-	C. Mono CD141+HLADR-	4	(4) C. Mono CD141+HLADR-
49	CyTOF C. Mono CD141+HLADR+	C. Mono CD141+HLADR+	27	(27) C. Mono CD141+HLADR+
50	CyTOF C. Mono CD16-	C. Mono CD16-	11	(11) C. Mono CD16-
51	CyTOF C. Mono CD16-CD11B-	C. Mono CD16-CD11B-	22	(22) C. Mono CD16-CD11B-
52	CyTOF C. Mono CD16-CD11B+	C. Mono CD16-CD11B+	9	(9) C. Mono CD16-CD11B+
53	CyTOF C. Mono CD16-CD169-	C. Mono CD16-CD169-	14	(14) C. Mono CD16-CD169-
54	CyTOF C. Mono CD16-CD169+	C. Mono CD16-CD169+	6	(6) C. Mono CD16-CD169+
55	CyTOF C. Mono CD16+	C. Mono CD16+	24	(24) C. Mono CD16+
56	CyTOF C. Mono CD16+CD11B-	C. Mono CD16+CD11B-	10	(10) C. Mono CD16+CD11B-
57	CyTOF C. Mono CD16+CD11B+	C. Mono CD16+CD11B+	26	(26) C. Mono CD16+CD11B+
58	CyTOF C. Mono CD16+CD169-	C. Mono CD16+CD169-	23	(23) C. Mono CD16+CD169-
59	CyTOF C. Mono CD16+CD169+	C. Mono CD16+CD169+	25	(25) C. Mono CD16+CD169+
60	CyTOF C. Mono CD169-HLADR-	C. Mono CD169-HLADR-	5	(5) C. Mono CD169-HLADR-
61	CyTOF C. Mono CD169-HLADR+	C. Mono CD169-HLADR+	28	(28) C. Mono CD169-HLADR+
62	CyTOF C. MONO CD169+	C. MONO CD169+	3	(3) C. Mono CD169+
63	CyTOF C. Mono CD169+HLADR-	C. Mono CD169+HLADR-	1	(1) C. Mono CD169+HLADR-
64	CyTOF C. Mono CD169+HLADR+	C. Mono CD169+HLADR+	29	(29) C. Mono CD169+HLADR+
65	CyTOF C. MONO CD38+	C. MONO CD38+	21	(21) C. Mono CD38+
66	CyTOF C. MONO CD45RA-	C. MONO CD45RA-	12	(12) C. Mono CD45RA-
67	CyTOF C. MONO CD45RA+	C. MONO CD45RA+	30	(30) C. Mono CD45RA+
68	CyTOF C. MONO CD56+	C. MONO CD56+	8	(8) C. Mono CD56+
69	CyTOF C. MONO CD86+	C. MONO CD86+	32	(32) C. Mono CD86+
70	CyTOF C. MONO IgA+	C. MONO IgA+	2	(2) C. Mono IgA+
71	CyTOF CD141+HLADR-Cells	CD141+HLADR-Cells	1	(1) CD141+HLADR- Cells
72	CyTOF CD16+ NK	CD16+ NK	1	(1) CD16+ NK
73	CyTOF CD16+ NK CD38+	CD16+ NK CD38+	2	(2) CD16+ NK CD38+
74	CyTOF CD4 CD11C+	CD4 CD11C+	10	(10) CD4 CD11C+
75	CyTOF CD4 CD127+	CD4 CD127+	18	(18) CD4 CD127+
76	CyTOF CD4 CD38+	CD4 CD38+	24	(24) CD4 CD38+
77	CyTOF CD4 CD57+	CD4 CD57+	33	(33) CD4 CD57+
78	CyTOF CD4 CXCR5-	CD4 CXCR5-	20	(20) CD4 CXCR5-
79	CyTOF CD4 CXCR5+	CD4 CXCR5+	13	(13) CD4 CXCR5+
80	CyTOF CD4 HLADR-CD38+CD45RO+	CD4 HLADR- CD38+CD45RO+	34	(34) CD4 HLADR-CD38+CD45RO+
81	CyTOF CD4 HLADR-CD38-	CD4 HLADR-CD38-	12	(12) CD4 HLADR-CD38-
82	CyTOF CD4 HLADR-CD38+	CD4 HLADR-CD38+	21	(21) CD4 HLADR-CD38+

83	CyTOF CD4 HLADR+ CD38+CD45RO+	CD4 HLADR+ CD38+CD45RO+	7	(7) CD4 HLADR+ CD38+CD45RO+
84	CyTOF CD4 HLADR+CD38-	CD4 HLADR+CD38-	1	(1) CD4 HLADR+CD38-
85	CyTOF CD4 HLADR+CD38+	CD4 HLADR+CD38+	30	(30) CD4 HLADR+CD38+
86	CyTOF CD4 NAIVE	CD4 NAIVE	15	(15) CD4 NAIVE
87	CyTOF CD4 NAIVE CD127+	CD4 NAIVE CD127+	16	(16) CD4 NAIVE CD127+
88	CyTOF CD4 NAIVE CD27+	CD4 NAIVE CD27+	14	(14) CD4 NAIVE CD27+
89	CyTOF CD4 NAIVE CD38+	CD4 NAIVE CD38+	4	(4) CD4 NAIVE CD38+
90	CyTOF CD4 T	CD4 T	19	(19) CD4 T
91	CyTOF CD4 TCM	CD4 TCM	27	(27) CD4 TCM
92	CyTOF CD4 TCM CD127+	CD4 TCM CD127+	22	(22) CD4 TCM CD127+
93	CyTOF CD4 TCM CD27+	CD4 TCM CD27+	25	(25) CD4 TCM CD27+
94	CyTOF CD4 TCM CD38+	CD4 TCM CD38+	28	(28) CD4 TCM CD38+
95	CyTOF CD4 TCM CD38+HLADR+	CD4 TCM CD38+HLADR+	3	(3) CD4 TCM CD38+HLADR+
96	CyTOF CD4 TEM	CD4 TEM	29	(29) CD4 TEM
97	CyTOF CD4 TEM CD127+	CD4 TEM CD127+	26	(26) CD4 TEM CD127+
98	CyTOF CD4 TEM CD38+	CD4 TEM CD38+	8	(8) CD4 TEM CD38+
99	CyTOF CD4 TEM CD38+HLADR+	CD4 TEM CD38+HLADR+	5	(5) CD4 TEM CD38+HLADR+
100	CyTOF CD4 TEMRA	CD4 TEMRA	17	(17) CD4 TEMRA
101	CyTOF CD4 TEMRA CD27-	CD4 TEMRA CD27-	2	(2) CD4 TEMRA CD27-
102	CyTOF CD4 TEMRA CD38+	CD4 TEMRA CD38+	31	(31) CD4 TEMRA CD38+
103	CyTOF CD4+ CD56- MAIT	CD4+ CD56- MAIT	6	(6) CD4+ CD56- MAIT
104	CyTOF CD4+ CD56- MAIT CD38+	CD4+ CD56- MAIT CD38+	9	(9) CD4+ CD56- MAIT CD38+
105	CyTOF CD4+ CD56+ MAIT	CD4+ CD56+ MAIT	23	(23) CD4+ CD56+ MAIT
106	CyTOF CD4+ CD56+ MAIT CD38+	CD4+ CD56+ MAIT CD38+	32	(32) CD4+ CD56+ MAIT CD38+
107	CyTOF CD4+CD25+	CD4+CD25+	11	(11) CD4+CD25+
108	CyTOF CD56 BRIGHT NK	CD56 BRIGHT NK	1	(1) CD56 BRIGHT NK
109	CyTOF CD56 BRIGHT NK CD11B+	CD56 BRIGHT NK CD11B+	4	(4) CD56 BRIGHT NK CD11B+
110	CyTOF CD56 BRIGHT NK CD11C+	CD56 BRIGHT NK CD11C+	6	(6) CD56 BRIGHT NK CD11C+
111	CyTOF CD56 BRIGHT NK CD38+	CD56 BRIGHT NK CD38+	5	(5) CD56 BRIGHT NK CD38+
112	CyTOF CD56 BRIGHT NK CD5+	CD56 BRIGHT NK CD5+	2	(2) CD56 BRIGHT NK CD5+
113	CyTOF CD56 BRIGHT NK HLADR+	CD56 BRIGHT NK HLADR+	3	(3) CD56 BRIGHT NK HLADR+
114	CyTOF CD56DIM NK	CD56DIM NK	1	(1) CD56DIM NK
115	CyTOF CD56DIM NK CD11B+	CD56DIM NK CD11B+	2	(2) CD56DIM NK CD11B+
116	CyTOF CD56DIM NK CD11C+	CD56DIM NK CD11C+	3	(3) CD56DIM NK CD11C+
117	CyTOF CD56DIM NK CD38+	CD56DIM NK CD38+	4	(4) CD56DIM NK CD38+
118	CyTOF CD56DIM NK CD5+	CD56DIM NK CD5+	5	(5) CD56DIM NK CD5+
119	CyTOF CD56DIM NK HLADR+	CD56DIM NK HLADR+	6	(6) CD56DIM NK HLADR+
120	CyTOF CD8 CD11C+	CD8 CD11C+	12	(12) CD8 CD11C+
121	CyTOF CD8 CD38+	CD8 CD38+	23	(23) CD8 CD38+
122	CyTOF CD8 CXCR5-	CD8 CXCR5-	16	(16) CD8 CXCR5-
123	CyTOF CD8 CXCR5+	CD8 CXCR5+	10	(10) CD8 CXCR5+
124	CyTOF CD8 HLADR-	CD8 HLADR- CD38+CD45RO+	24	(24) CD8 HLADR-

	CD38+CD45RO+			CD38+CD45RO+
125	CyTOF CD8 HLADR-CD38-	CD8 HLADR-CD38-	6	(6) CD8 HLADR-CD38-
126	CyTOF CD8 HLADR-CD38+	CD8 HLADR-CD38+	21	(21) CD8 HLADR-CD38+
127	CyTOF CD8 HLADR+ CD38+CD45RO+	CD8 HLADR+ CD38+CD45RO+	26	(26) CD8 HLADR+ CD38+CD45RO+
128	CyTOF CD8 HLADR+CD38-	CD8 HLADR+CD38-	1	(1) CD8 HLADR+CD38-
129	CyTOF CD8 HLADR+CD38+	CD8 HLADR+CD38+	28	(28) CD8 HLADR+CD38+
130	CyTOF CD8 NAIVE	CD8 NAIVE	15	(15) CD8 NAIVE
131	CyTOF CD8 NAIVE CD127+	CD8 NAIVE CD127+	19	(19) CD8 NAIVE CD127+
132	CyTOF CD8 NAIVE CD27+	CD8 NAIVE CD27+	17	(17) CD8 NAIVE CD27+
133	CyTOF CD8 NAIVE CD38+	CD8 NAIVE CD38+	7	(7) CD8 NAIVE CD38+
134	CyTOF CD8 T CELL	CD8 T CELL	13	(13) CD8 T CELL
135	CyTOF CD8 TCM CD127+	CD8 TCM CD127+	5	(5) CD8 TCM CD127+
136	CyTOF CD8 TCM CD27+	CD8 TCM CD27+	14	(14) CD8 TCM CD27+
137	CyTOF CD8 TCM CD38+	CD8 TCM CD38+	29	(29) CD8 TCM CD38+
138	CyTOF CD8 TCM CD38+HLADR+	CD8 TCM CD38+HLADR+	27	(27) CD8 TCM CD38+HLADR+
139	CyTOF CD8 TEM	CD8 TEM	20	(20) CD8 TEM
140	CyTOF CD8 TEM CD127+	CD8 TEM CD127+	3	(3) CD8 TEM CD127+
141	CyTOF CD8 TEM CD27+	CD8 TEM CD27+	22	(22) CD8 TEM CD27+
142	CyTOF CD8 TEM CD38+	CD8 TEM CD38+	30	(30) CD8 TEM CD38+
143	CyTOF CD8 TEM CD38+HLADR+	CD8 TEM CD38+HLADR+	25	(25) CD8 TEM CD38+HLADR+
144	CyTOF CD8 TEMRA	CD8 TEMRA	8	(8) CD8 TEMRA
145	CyTOF CD8 TEMRA CD127+	CD8 TEMRA CD127+	2	(2) CD8 TEMRA CD127+
146	CyTOF CD8 TEMRA CD27-	CD8 TEMRA CD27-	4	(4) CD8 TEMRA CD27-
147	CyTOF CD8 TEMRA CD38+	CD8 TEMRA CD38+	11	(11) CD8 TEMRA CD38+
148	CyTOF CD8+ CD25+	CD8+ CD25+	9	(9) CD8+ CD25+
149	CyTOF CD8+ CD56- MAIT	CD8+ CD56- MAIT	2	(2) MAIT CD8+ CD56-
150	CyTOF CD8+ CD56- MAIT CD38+	CD8+ CD56- MAIT CD38+	1	(1) MAIT CD8+ CD56- CD38+
151	CyTOF CD8+ CD56+ MAIT	CD8+ CD56+ MAIT	5	(5) MAIT CD8+ CD56+
152	CyTOF CD8+ CD56+ MAIT CD38+	CD8+ CD56+ MAIT CD38+	10	(10) MAIT CD8+ CD56+ CD38+
153	CyTOF CD8+ TCM	CD8+ TCM	18	(18) CD8+ TCM
154	CyTOF cDC1	cDC1	7	(7) cDC1
155	CyTOF cDC1 CD38+	cDC1 CD38+	8	(8) cDC1 CD38+
156	CyTOF cDC2	cDC2	2	(2) cDC2
157	CyTOF cDC2 CD11B+	cDC2 CD11B+	6	(6) cDC2 CD11B+
158	CyTOF cDC2 CD38+	cDC2 CD38+	3	(3) cDC2 CD38+
159	CyTOF cDC2 CD5-	cDC2 CD5-	4	(4) cDC2 CD5-
160	CyTOF cDC2 CD5+	cDC2 CD5+	5	(5) cDC2 CD5+
161	CyTOF CSM	CSM	43	(43) B CSM
162	CyTOF CSM CCR6-	CSM CCR6-	29	(29) B CSM CCR6-
163	CyTOF CSM CCR6+	CSM CCR6+	39	(39) B CSM CCR6+
164	CyTOF CSM CXCR5-	CSM CXCR5-	31	(31) B CSM CXCR5-
165	CyTOF CSM CXCR5+	CSM CXCR5+	38	(38) B CSM CXCR5+

166	CyTOF DC	DC	1	(1) DC
167	CyTOF DC4	DC4	9	(9) cDC4
168	CyTOF DC4 CD38+	DC4 CD38+	10	(10) cDC4 CD38+
169	CyTOF DN CD56- MAIT	DN CD56- MAIT	3	(3) MAIT DN CD56-
170	CyTOF DN CD56- MAIT CD38+	DN CD56- MAIT CD38+	6	(6) MAIT DN CD56- CD38+
171	CyTOF DN CD56+ MAIT	DN CD56+ MAIT	4	(4) MAIT DN CD56+
172	CyTOF DN CD56+ MAIT CD38+	DN CD56+ MAIT CD38+	11	(11) MAIT DN CD56+ CD38+
173	CyTOF ICOS+ TFH	ICOS+ TFH	3	(3) TFH ICOS+
174	CyTOF ILC1	ILC1	5	(5) ILC1
175	CyTOF ILC1 CD25-	ILC1 CD25-	6	(6) ILC1 CD25-
176	CyTOF ILC1 CD25+	ILC1 CD25+	7	(7) ILC1 CD25+
177	CyTOF ILC1 CD38+	ILC1 CD38+	8	(8) ILC1 CD38+
178	CyTOF ILC2	ILC2	1	(1) ILC2
179	CyTOF ILC2 CD25-	ILC2 CD25-	2	(2) ILC2 CD25-
180	CyTOF ILC2 CD25+	ILC2 CD25+	3	(3) ILC2 CD25+
181	CyTOF ILC2 CD38+	ILC2 CD38+	4	(4) ILC2 CD38+
182	CyTOF ILC3	ILC3	9	(9) ILC3
183	CyTOF ILC3 CD25-	ILC3 CD25-	10	(10) ILC3 CD25-
184	CyTOF ILC3 CD25+	ILC3 CD25+	11	(11) ILC3 CD25+
185	CyTOF INT. MONO	INT. MONO	14	(14) INT. Mono
186	CyTOF Int. Mono CD141-	Int. Mono CD141-	24	(24) INT. Mono CD141-
187	CyTOF Int. Mono CD141-CD11B-	Int. Mono CD141-CD11B-	18	(18) INT. Mono CD141-CD11B-
188	CyTOF Int. Mono CD141-CD11B+	Int. Mono CD141-CD11B+	17	(17) INT. Mono CD141-CD11B+
189	CyTOF Int. Mono CD141-HLADR-	Int. Mono CD141-HLADR-	7	(7) INT. Mono CD141-HLADR-
190	CyTOF Int. Mono CD141-HLADR+	Int. Mono CD141-HLADR+	21	(21) INT. Mono CD141-HLADR+
191	CyTOF Int. Mono CD141+	Int. Mono CD141+	11	(11) INT. Mono CD141+
192	CyTOF Int. Mono CD141+CD11B-	Int. Mono CD141+CD11B-	10	(10) INT. Mono CD141+CD11B-
193	CyTOF Int. Mono CD141+CD11B+	Int. Mono CD141+CD11B+	16	(16) INT. Mono CD141+CD11B+
194	CyTOF Int. Mono CD141+HLADR-	Int. Mono CD141+HLADR-	2	(2) INT. Mono CD141+HLADR-
195	CyTOF Int. Mono CD141+HLADR+	Int. Mono CD141+HLADR+	19	(19) INT. Mono CD141+HLADR+
196	CyTOF Int. Mono CD16+	Int. Mono CD16+	8	(8) INT. Mono CD16+
197	CyTOF Int. Mono CD16++	Int. Mono CD16++	22	(22) INT. Mono CD16++
198	CyTOF Int. Mono CD16+CD11B-	Int. Mono CD16+CD11B-	13	(13) INT. Mono CD16+CD11B-
199	CyTOF Int. Mono CD16+CD11B+	Int. Mono CD16+CD11B+	15	(15) INT. Mono CD16+CD11B+
200	CyTOF Int. Mono CD16+CD169-	Int. Mono CD16+CD169-	9	(9) INT. Mono CD16+CD169-
201	CyTOF Int. Mono CD16+CD169+	Int. Mono CD16+CD169+	25	(25) INT. Mono CD16+CD169+
202	CyTOF Int. Mono CD169-HLADR-	Int. Mono CD169-HLADR-	4	(4) INT. Mono CD169-HLADR-
203	CyTOF Int. Mono CD169-HLADR+	Int. Mono CD169-HLADR+	12	(12) INT. Mono CD169-HLADR+
204	CyTOF INT. MONO CD169+	INT. MONO CD169+	23	(23) INT. Mono CD169+

205	CyTOF Int. Mono CD169+HLADR-	Int. Mono CD169+HLADR-	1	(1) INT. Mono CD169+HLADR-
206	CyTOF Int. Mono CD169+HLADR+	Int. Mono CD169+HLADR+	26	(26) INT. Mono CD169+HLADR+
207	CyTOF INT. MONO CD38+	INT. MONO CD38+	20	(20) INT. Mono CD38+
208	CyTOF INT. MONO CD45RA-	INT. MONO CD45RA-	6	(6) INT. Mono CD45RA-
209	CyTOF INT. MONO CD45RA+	INT. MONO CD45RA+	28	(28) INT. Mono CD45RA+
210	CyTOF INT. MONO CD56+	INT. MONO CD56+	5	(5) INT. Mono CD56+
211	CyTOF INT. MONO CD86+	INT. MONO CD86+	27	(27) INT. Mono CD86+
212	CyTOF INT. MONO IgA+	INT. MONO IgA+	3	(3) INT. Mono IgA+
213	CyTOF LD Neu	LD Neu	1	(1) LD Neu
214	CyTOF LD Neu CD38+	LD Neu CD38+	2	(2) LD Neu CD38+
215	CyTOF LD Neu CD5+	LD Neu CD5+	3	(3) LD Neu CD5+
216	CyTOF LD Neu IgA+	LD Neu IgA+	4	(4) LD Neu IgA+
217	CyTOF LD Neu PD-L1+	LD Neu PD-L1+	5	(5) LD Neu PD-L1+
218	CyTOF MAIT	MAIT	8	(8) MAIT
219	CyTOF MAIT CD38+	MAIT CD38+	13	(13) MAIT CD38+
220	CyTOF MAIT CD56-	MAIT CD56-	9	(9) MAIT CD56-
221	CyTOF MAIT CD56- CD38+	MAIT CD56- CD38+	14	(14) MAIT CD56- CD38+
222	CyTOF MAIT CD56+	MAIT CD56+	7	(7) MAIT CD56+
223	CyTOF MAIT CD56+ CD38+	MAIT CD56+ CD38+	12	(12) MAIT CD56+ CD38+
224	CyTOF NC. MONO	NC. MONO	16	(16) NC. Mono
225	CyTOF NC. MONO CCR7-	NC. MONO CCR7-	17	(17) NC. Mono CCR7-
226	CyTOF NC. MONO CCR7+	NC. MONO CCR7+	6	(6) NC. Mono CCR7+
227	CyTOF NC. MONO CD123+	NC. MONO CD123+	13	(13) NC. Mono CD123+
228	CyTOF NC. Mono CD141-	NC. Mono CD141-	20	(20) NC. Mono CD141-
229	CyTOF NC. Mono CD141-CD11B-	NC. Mono CD141-CD11B-	8	(8) NC. Mono CD141-CD11B-
230	CyTOF NC. Mono CD141-CD11B+	NC. Mono CD141-CD11B+	24	(24) NC. Mono CD141-CD11B+
231	CyTOF NC. Mono CD141-HLADR-	NC. Mono CD141-HLADR-	2	(2) NC. Mono CD141-HLADR-
232	CyTOF NC. Mono CD141-HLADR+	NC. Mono CD141-HLADR+	21	(21) NC. Mono CD141-HLADR+
233	CyTOF NC. Mono CD141+	NC. Mono CD141+	14	(14) NC. Mono CD141+
234	CyTOF NC. Mono CD141+CD11B-	NC. Mono CD141+CD11B-	1	(1) NC. Mono CD141+CD11B-
235	CyTOF NC. Mono CD141+CD11B+	NC. Mono CD141+CD11B+	23	(23) NC. Mono CD141+CD11B+
236	CyTOF NC. Mono CD141+HLADR-	NC. Mono CD141+HLADR-	7	(7) NC. Mono CD141+HLADR-
237	CyTOF NC. Mono CD141+HLADR+	NC. Mono CD141+HLADR+	15	(15) NC. Mono CD141+HLADR+
238	CyTOF NC. Mono CD16++	NC. Mono CD16++	19	(19) NC. Mono CD16++
239	CyTOF NC. Mono CD16+CD11B-	NC. Mono CD16+CD11B-	4	(4) NC. Mono CD16+CD11B-
240	CyTOF NC. Mono CD16+CD11B+	NC. Mono CD16+CD11B+	25	(25) NC. Mono CD16+CD11B+
241	CyTOF NC. Mono CD16+CD169-	NC. Mono CD16+CD169-	12	(12) NC. Mono CD16+CD169-
242	CyTOF NC. Mono CD16+CD169+	NC. Mono CD16+CD169+	29	(29) NC. Mono CD16+CD169+

243	CyTOF NC. Mono CD169-HLADR-	NC. Mono CD169-HLADR-	5	(5) NC. Mono CD169-HLADR-
244	CyTOF NC. Mono CD169-HLADR+	NC. Mono CD169-HLADR+	11	(11) NC. Mono CD169-HLADR+
245	CyTOF NC. Mono CD169+HLADR-	NC. Mono CD169+HLADR-	18	(18) NC. Mono CD169+HLADR-
246	CyTOF NC. Mono CD169+HLADR+	NC. Mono CD169+HLADR+	27	(27) NC. Mono CD169+HLADR+
247	CyTOF NC. Mono CD16lo	NC. Mono CD16lo	9	(9) NC. Mono CD16lo
248	CyTOF NC. MONO CD38+	NC. MONO CD38+	26	(26) NC. Mono CD38+
249	CyTOF NC. MONO CD45RO-	NC. MONO CD45RO-	3	(3) NC. Mono CD45RO-
250	CyTOF NC. MONO CD45RO+	NC. MONO CD45RO+	30	(30) NC. Mono CD45RO+
251	CyTOF NC. MONO CD56+	NC. MONO CD56+	22	(22) NC. Mono CD56+
252	CyTOF NC. MONO CD86+	NC. MONO CD86+	10	(10) NC. Mono CD86+
253	CyTOF NC. MONO IgA+	NC. MONO IgA+	28	(28) NC. Mono IgA+
254	CyTOF NK CD11B+	NK CD11B+	1	(1) NK CD11B+
255	CyTOF NK CD11C+	NK CD11C+	2	(2) NK CD11C+
256	CyTOF NKT	NKT	1	(1) NKT
257	CyTOF NKT CD161-	NKT CD161-	2	(2) NKT CD161-
258	CyTOF NKT CD161+	NKT CD161+	3	(3) NKT CD161+
259	CyTOF NKT CD38+	NKT CD38+	4	(4) NKT CD38+
260	CyTOF NKT CD57-	NKT CD57-	5	(5) NKT CD57-
261	CyTOF NKT CD57-CD4+	NKT CD57-CD4+	6	(6) NKT CD57-CD4+
262	CyTOF NKT CD57-CD8+	NKT CD57-CD8+	7	(7) NKT CD57-CD8+
263	CyTOF NKT CD57-DN	NKT CD57-DN	8	(8) NKT CD57-DN
264	CyTOF NKT CD57-DP	NKT CD57-DP	9	(9) NKT CD57-DP
265	CyTOF NKT CD57+	NKT CD57+	10	(10) NKT CD57+
266	CyTOF NKT CD57+CD4+	NKT CD57+CD4+	11	(11) NKT CD57+CD4+
267	CyTOF NKT CD57+CD8+	NKT CD57+CD8+	12	(12) NKT CD57+CD8+
268	CyTOF NKT CD57+DN	NKT CD57+DN	13	(13) NKT CD57+DN
269	CyTOF NKT CD57+DP	NKT CD57+DP	14	(14) NKT CD57+DP
270	CyTOF NSM	NSM	14	(14) B NSM
271	CyTOF NSM CD27+CD38-	NSM CD27+CD38-	6	(6) B NSM CD27+CD38-
272	CyTOF NSM CD27+CD38+	NSM CD27+CD38+	13	(13) B NSM CD27+CD38+
273	CyTOF NSM CD38+	NSM CD38+	23	(23) B NSM CD38+
274	CyTOF PDC	PDC	1	(1) PDC
275	CyTOF PDC CD45RA+	PDC CD45RA+	2	(2) PDC CD45RA+
276	CyTOF PDC CD45RA+CD38++	PDC CD45RA+CD38high	3	(3) PDC CD45RA+CD38++
277	CyTOF PLASMABLASTS	PLASMABLASTS	3	(3) PLASMABL.
278	CyTOF PLASMABLASTS CXCR5-	PLASMABLASTS CXCR5-	2	(2) PLASMABL. CXCR5-
279	CyTOF PLASMABLASTS CXCR5+	PLASMABLASTS CXCR5+	5	(5) PLASMABL. CXCR5+
280	CyTOF PLASMABLASTS IgA-	PLASMABLASTS IgA-	1	(1) PLASMABL. IgA-
281	CyTOF PLASMABLASTS IgA+	PLASMABLASTS IgA+	4	(4) PLASMABL. IgA+
282	CyTOF T CD38+	T CD38+	6	(6) T CD38+
283	CyTOF T cells	T cells	3	(3) T cells

284	CyTOF T cells CCR7-	T cells CCR7-	1	(1) T CCR7-
285	CyTOF T cells CCR7+	T cells CCR7+	5	(5) T CCR7+
286	CyTOF T CXCR5-	T CXCR5-	4	(4) T CXCR5-
287	CyTOF T CXCR5+	T CXCR5+	2	(2) T CXCR5+
288	CyTOF TFH	TFH	1	(1) TFH
289	CyTOF TFH CD38+	TFH CD38+	2	(2) TFH CD38+
290	CyTOF TRANS	TRANS	11	(11) B TRANS
291	CyTOF TRANS CCR6-	TRANS CCR6-	44	(44) B TRANS CCR6-
292	CyTOF TRANS CCR6+	TRANS CCR6+	9	(9) B TRANS CCR6+
293	CyTOF TRANS CD5-	TRANS CD5-	4	(4) B TRANS CD5-
294	CyTOF TRANS CD5+	TRANS CD5+	21	(21) B TRANS CD5+
295	CyTOF TREG	TREG	3	(3) TREG
296	CyTOF TREG CD11C+	TREG CD11C+	1	(1) TREG CD11C+
297	CyTOF TREG CD38+	TREG CD38+	11	(11) TREG CD38+
298	CyTOF TREG CD45RO-ICOS+CD127+	TREG CD45RO-ICOS+CD127+	6	(6) TREG CD45RO-ICOS+CD127+
299	CyTOF TREG CD45RO+ICOS+CD127+	TREG CD45RO+ICOS+CD127+	9	(9) TREG CD45RO+ICOS+CD127+
300	CyTOF TREG ICOS+	TREG ICOS+	7	(7) TREG ICOS+
301	CyTOF TREG NAIVE	TREG NAIVE	4	(4) TREG NAIVE
302	CyTOF TREG NAIVE CD38+	TREG NAIVE CD38+	5	(5) TREG NAIVE CD38+
303	CyTOF TREG TCM	TREG TCM	2	(2) TREG TCM
304	CyTOF TREG TCM CD38+	TREG TCM CD38+	10	(10) TREG TCM CD38+
305	CyTOF TREG TEM	TREG TEM	8	(8) TREG TEM
306	CyTOF TREG TEM CD38+	TREG TEM CD38+	13	(13) TREG TEM CD38+
307	CyTOF TREG TEMRA	TREG TEMRA	12	(12) TREG TEMRA
308	CyTOF VD1	VD1	11	(11) VD1
309	CyTOF VD1 CD38+	VD1 CD38+	12	(12) VD1 CD38+
310	CyTOF VD1 NAIVE	VD1 NAIVE	13	(13) VD1 NAIVE
311	CyTOF VD1 NAIVE CD38+	VD1 NAIVE CD38+	14	(14) VD1 NAIVE CD38+
312	CyTOF VD1 TCM	VD1 TCM	15	(15) VD1 TCM
313	CyTOF VD1 TCM CD38+	VD1 TCM CD38+	16	(16) VD1 TCM CD38+
314	CyTOF VD1 TEM	VD1 TEM	17	(17) VD1 TEM
315	CyTOF VD1 TEM CD38+	VD1 TEM CD38+	18	(18) VD1 TEM CD38+
316	CyTOF VD1 TEMRA	VD1 TEMRA	19	(19) VD1 TEMRA
317	CyTOF VD1 TEMRA CD38+	VD1 TEMRA CD38+	20	(20) VD1 TEMRA CD38+
318	CyTOF VD2	VD2	1	(1) VD2
319	CyTOF VD2 CD38++	VD2 CD38high	2	(2) VD2 CD38++
320	CyTOF VD2 NAIVE	VD2 NAIVE	3	(3) VD2 NAIVE
321	CyTOF VD2 NAIVE CD38+	VD2 NAIVE CD38+	4	(4) VD2 NAIVE CD38+
322	CyTOF VD2 TCM	VD2 TCM	5	(5) VD2 TCM
323	CyTOF VD2 TCM CD38+	VD2 TCM CD38+	6	(6) VD2 TCM CD38+
324	CyTOF VD2 TEM	VD2 TEM	7	(7) VD2 TEM

325	CyTOF VD2 TEM CD38+	VD2 TEM CD38+	8	(8) VD2 TEM CD38+
326	CyTOF VD2 TEMRA	VD2 TEMRA	9	(9) VD2 TEMRA
327	CyTOF VD2 TEMRA CD38+	VD2 TEMRA CD38+	10	(10) VD2 TEMRA CD38+

Table S3. Definition of nodes used in timing and severity COVID-19 networks.